Bioactive Materials 18 (2022) 300–320

Contents lists available at ScienceDirect

Bioactive Materials

journal homepage: www.keaipublishing.com/en/journals/bioactive-materials

Acellular nerve xenografts based on supercritical extraction technology for repairing long-distance sciatic nerve defects in rats

Shuai Wei [a,b,c,1], Qian Hu [d,1], Jianxiong Ma [a,e,1], Xiu Dai [c], Yu Sun [c], Gonghai Han [f], Haoye Meng [b], Wenjing Xu [b], Lei Zhang [g], Xinlong Ma [a,e,***], Jiang Peng [b,**], Yu Wang [b,c,*]

[a] Tianjin Hospital, Tianjin University, No. 406 Jiefang South Road, Hexi District, Tianjin, 300211, China
[b] Institute of Orthopedics, The First Medical Center, Chinese PLA General Hospital, Beijing Key Lab of Regenerative Medicine in Orthopedics, Key Laboratory of Musculoskeletal Trauma and War Injuries PLA, No.28 Fuxing Road, Haidian District, Beijing 100853, China
[c] Key Laboratory of Neuroregeneration of Jiangsu and Ministry of Education, Neural Regeneration Co-Innovation Center of Jiangsu Province, Nantong University, No. 19 Qixiu Road, Chongchuan District, Nantong, 226001, China
[d] Department of Geriatrics, The Second People's Hospital of Nantong, Affiliated Rehabilitation Hospital of Nantong University, No. 298 Xinhua Road, Chongchuan District, Nantong, 226006, China
[e] Institute of Orthopedics, Tianjin Hospital Tianjin University, Tianjin Key Laboratory of Orthopedic Biomechanics and Medical Engineering, No. 155 Munan Road, Heping District, Tianjin, 300050, China
[f] The First People's Hospital of Yunnan Province, No. 157 Jinbi Road, Xishan District, Kunming, 650034, China
[g] Academy of Medical Engineering and Translational Medicine, Tianjin University, No. 92 Weijin Road, Nankai District, Tianjin, 300072, China

ARTICLE INFO

Keywords:
Peripheral nerve regeneration
Acellular nerve xenograft
Supercritical extraction
Peripheral nerve injury
Nerve defect

ABSTRACT

Compared to conventional artificial nerve guide conduits (NGCs) prepared using natural polymers or synthetic polymers, acellular nerve grafts (ACNGs) derived from natural nerves with eliminated immune components have natural bionic advantages in composition and structure that polymer materials do not have. To further optimize the repair effect of ACNGs, in this study, we used a composite technology based on supercritical carbon dioxide ($scCO_2$) extraction to process the peripheral nerve of a large mammal, the Yorkshire pig, and obtained an innovative Acellular nerve xenografts (ANXs, namely, CD + $scCO_2$ NG). After $scCO_2$ extraction, the fat and DNA content in CD + $scCO_2$ NG has been removed to the greatest extent, which can better supported cell adhesion and proliferation, inducing an extremely weak inflammatory response. Interestingly, the protein in the CD + $scCO_2$ NG was primarily involved in signaling pathways related to axon guidance. Moreover, compared with the pure chemical decellularized nerve graft (CD NG), the DRG axons grew naturally on the CD + $scCO_2$ NG membrane and extended long distances. In vivo studies further revealed that the regenerated nerve axons had basically crossed the CD + $scCO_2$ NG 3 weeks after surgery. 12 weeks after surgery, CD + scCO2 NG was similar to autologous nerves in improving the quality of nerve regeneration, target muscle morphology and motor function recovery and was significantly better than hollow NGCs and CD NG. Therefore, we believe that the fully decellularized and fat-free porcine ACNGs may be the most promising "bridge" for repairing human nerve defects at this stage and for some time to come.

1. Introduction

A bridge, as the name suggests, is a structure used to overcome obstacles. There are many famous bridges in the world that not only bring convenience to people's lives but that also from beautiful scenery. In the medical field, we often hear "heart bypass". Similarly, when the peripheral nerve suffers severe damage and there is a defect, we need to provide a bridge for it. Peripheral nerve injury (PNI) is a common

Peer review under responsibility of KeAi Communications Co., Ltd.
* Corresponding author. Senior department of Orthopedics, Beijing Key Lab of Regenerative Medicine in Orthopedics, The 1st Medical Centre of PLA General Hospital, No. 28 Fuxing Road, Haidian District, Beijing, 100853, China.
** Corresponding author.
*** Corresponding author. Tianjin Hospital, Tianjin University, No. 406 Jiefang South Road, Hexi District, Tianjin 300211, China.
E-mail addresses: maxinlong8686@sina.com (X. Ma), pengjiang301@126.com (J. Peng), wangwangdian628@126.com (Y. Wang).
[1] Shuai Wei, Qian Hu, and Jianxiong Ma contributed equally to this work.

https://doi.org/10.1016/j.bioactmat.2022.03.014
Received 18 January 2022; Received in revised form 20 February 2022; Accepted 8 March 2022
Available online 18 March 2022

clinical condition [1]. Approximately 1 million PNIs occur worldwide every year [2]. These injuries convey a serious economic burden to society and lead to the loss of limbs or organ functions, which greatly affects patient quality of life [3,4]. More serious PNI is often accompanied by a certain degree of nerve defect, and clinicians will choose a "bridge" to fill it.

For many years, autologous nerve transplantation has been the clinical "gold standard" for the treatment of nerve defects [3]. While obtaining satisfactory repair results, autologous nerve transplantation also exhibits scveral shortcomings, such as differences in nerve size, secondary dysfunction in the donor area, and a risk of neuroma formation along with insufficient donor sources [5,6]. When the "bridges" derived from the patients themselves became subject to various restrictions, scholars turned their attention to artificial nerve guidance conduits (NGCs). Thus far, the U.S. Food and Drug Administration (FDA) has approved some NGCs for clinical application that have shown positive therapeutic effects, such as NeuraGen and Neurolac [7–9]. However, most current NGCs are hollow and have catheter structures, which do not accurately simulate the three-dimensional anisotropic structure of natural nerves [10,11]. At the same time, the composition is also significantly different from that of natural nerve extracellular matrix (ECM). To overcome the abovementioned challenges, researchers have used advanced manufacturing technology to create complex NGCs to simulate the internal structure of autologous nerves [3,12–15], primarily including the following 4 designs: porous, grooved, multichannel and NGCs with fillers (fiber or hydrogel) [16]. Compared to the hollow catheter structure, the abovementioned complex design has indeed achieved a more satisfactory repair effect, but its structure is still far from the three-dimensional anisotropic structure of the natural nerve [17–19]. With the emergence and further development of technologies and materials, such as 4D printing, intelligent materials and modular fabrication, a new generation of bionic NGCs will inevitably be comparable to natural nerves in structure, composition and function [20–22]. In addition, with the development of gene editing technology, cell transplantation has brought hope to patients for the treatment of hematopoietic diseases [23,24]. Therefore, we have reason to believe that xenotransplantation (liver, kidney, nerve and bone tissue) based on gene editing technology will also become reality in the near future.

At this stage, the "bridge" closest to natural nerves in structure and composition is acellular nerve grafts (ACNGs), which are a very promising alternative to autologous nerve grafts (ANGs) [1,25]. ANGs remove components that cause immune rejection, such as cells, myelin sheaths and axons, while retaining the three-dimensional oriented neural basement membrane tube structure that can guide nerve regeneration [26], providing a scaffold for immediate cell migration and angiogenesis [27,28]. A recent study indicated that approximately 70% of American hand surgeons have used ANGs in surgery to repair nerve defects [29]. Scholars have made various attempts to obtain qualified ANGs, such as irradiation, repeated freeze-thaw cycles and detergent treatment [30–32]. However, ANGs prepared based on these methods do not preserve the three-dimensional ECM structure very well, and residual cellular debris is an obstacle to axon regeneration that inevitably causes strong immune rejection by the host. Compared to other methods, the chemical reagent washing and decellularization scheme does have certain advantages, and the chemical decellularization (CD) scheme developed by Johnson et al. is the most commonly used [33]. Based on this method, Sondell et al. created a scheme consisting of Triton X-100 and sodium deoxycholate, which has more advantages for preserving the internal structure of natural nerves [34]. The allograft prepared based on the Sondell protocol has been demonstrated to effectively remove cellular components and achieve satisfactory nerve regeneration in vivo. Six years later, Hudson et al. proposed a less corrosive CD method based on Triton X-200 and sulfobetaine-10 and -16 (SB-10, SB-16) [35]. SB-10 and SB-16 are zwitterionic detergents that have the characteristics of nonionic and ionic detergents and have more advantages in maintaining the integrity of the ECM [36]. In addition, the only ANG-Axogen approved by the US Food and Drug Administration is based on the Hudson protocol, and its clinical repair effect is satisfactory and superior to commercial NGCs [37,38]. However, due to various factors, the previously commercialized Triton X-200 detergent has been discontinued and is difficult to synthesize locally [39]. At the same time, the use of a variety of chemical detergents increases the possibility of chemical residues in ANGs, inducing more intense cytotoxicity [40]. Therefore, it is necessary to explore decellularization methods with equivalent or improved effects.

As a green and environmentally friendly technology, $scCO_2$ extraction is favored and plays an important role in many applications, such as solving environmental pollution [41], extracting natural products [42], preparing nanoparticles [43], material processing [44] and sterilizing [45]. As an environmentally friendly solvent, CO_2 has the advantages of nontoxicity, low cost and easy recycling [44,46,47]. The mild supercritical state parameters of CO_2 (critical pressure 7.38 MPa; critical temperature 31 °C) ensure that $scCO_2$ can also play an important role in the field of biomedicine and biomaterials [48]. Under such high pressure and low temperature conditions, $scCO_2$ exhibits the characteristics of low viscosity and high diffusivity, which allows penetration of dense materials and acts as a powerful solvent [49,50]. Carbon dioxide exhibits unique advantages in dissolving organic compounds, especially some lipophilic compounds. The first application of $scCO_2$ in the biomedical industry was to extract lipids from bone scaffolds, maintaining the strength of the bone scaffolds while reducing their antigenicity [51]. In addition, SC-CO2 is also used to decellularize porcine aorta [52], porcine corneal tissue [53] and rat heart tissue [54].

In terms of the selection of raw materials for the preparation of ACNGs, most are related to allogeneic ACNG research, and some have been approved by the FDA and used in clinical applications [55]. However, due to trauma and disease, there are many peripheral nerve tissues derived from the human body that cannot be collected. In addition, due to religious and cultural issues, it has become difficult to obtain nerve tissue from human cadavers in some countries. In many studies, most of the ECM scaffolds used for surgical reconstruction come from mammals, such as skin, tendons, blood vessels and nerves [56]. Compared with allografts, the sources of xenografts are more extensive, and their use avoids religious and cultural issues. In terms of the source of acellular nerve xenografts (ANXs) with the most promising clinical transformation, we believe that peripheral nerve tissue derived from porcine species is the most suitable [57] for three reasons: I) peripheral nerves derived from porcine are more compatible with humans in terms of anatomical structure and diameter; II) compared to most mammals, porcine and humans have higher genetic homology and are more emotionally acceptable; III) pig breeding technology is mature, and their nerve source is rich, easy to obtain and has low economic cost. However, peripheral nerves derived from porcine sources are thicker in diameter, and the epineurium is dense and contains more nerve bundles, preventing the conventional decellularization protocol from achieving the desired effect [58]. In addition, porcine nerves are rich in lipids, which may hinder the production of qualified ACNGs for a number of reasons. I) The phospholipid bilayer structure of the cell membrane hinders the removal of intracellular antigenic substances (nucleic acids and some proteins). II) Some lipids anchored on membrane proteins participate in the immune response [59]. III) Some lipids may promote the occurrence of inflammation [60]. Ⅳ) Lipids also hinder the recellularization of ACNG after transplantation through their hydrophobic property [61]. Ⅴ) Lipids may interfere with the conduction of electrical signals during the process of nerve regeneration. In terms of decellularization and defatting of pig nerves, we hypothesize that green and environmentally friendly supercritical carbon dioxide extraction technology may convey a unique advantage. It should be noted that chemical detergents still play a pivotal role in the preparation of ECM scaffolds. A recent study demonstrated that a decellularization program based on the mild chemical detergent sodium dodecyl sulfonate (SDS) provides a reference for preparing qualified ACNG from porcine [62]. However, the role of

chemical detergents in degreasing is very limited.

In the present study, for peripheral nerves derived from porcine species, we attempted to prepare a new type of ANXs based on very low concentrations of chemical detergents combined with $scCO_2$ extraction. The results showed that the fat of the new ANXs was removed to the greatest extent, and its DNA content was also reduced to below clinical standards. At the same time, the well-preserved three-dimensional directional nerve basement membrane tube structure could better guide and promote the growth of nerve axons. In vivo experiments on repairing long sciatic nerve defects in rats illustrated that the effect approximated autologous nerve transplantation. Based on the above findings, we believe that the fully decellularized and fat-free porcine ACNG may be the most promising "bridge" for repairing human nerve defects at this stage and for some time to come. In addition, we hope that this new type of ANXs based on multifield technology provides scientists with some enlightenment for the design of the next generation of artificial NGCs and the advancement of xenogeneic acellular nerve grafts for clinical application as soon as possible.

2. Materials and methods

2.1. Preparation of ANXs

Fresh sciatic nerves from adult Yorkshire pigs weighing 200–250 kg were obtained from a qualified animal slaughterhouse approved by the local government. Under aseptic conditions, the visible fat and connective tissue around the nerves were removed (Fig. 1A), and the nerves were washed three times in deionized water for 5 min each. For the specific decellularization and defatting process, please refer to the Chinese patent (original Patent No. ZL 2018 1 1331708. X) published by our team. A brief processing flow is shown in Fig. 1 as well. Briefly, the nerve tissue obtained in the above steps was repeatedly frozen and thawed three times (−80 °C–37 °C) and then treated with 0.5% sodium dodecyl sulfonate (SDS; L6026, Sigma–Aldrich, USA) extract in an orbital shaker for 48 h at 4 °C (Fig. 1B). Next, the nerve tissue was intermittently treated in an ultrasound instrument (Sigma–Aldrich, USA) 3 times for 3 min each at a frequency of 50000 Hz, shaken and cleaned in sterile saline (Solarbio, China) in an orbital shaker (Thermo Fisher Scientific, USA) for 60 h, and the saline was changed every 6 h. To further remove the DNA material remaining in the interstitial space, the isolated nerve was treated with 60 u/ml DNAse I (D5025, Sigma–Aldrich, USA) and 2 u/ml RNAse A (R4875, Sigma–Aldrich, USA) solution at 37 °C for 5 h and then washed according to the above conditions and replaced with saline. At this time, we obtained pure chemical decellularized sciatic nerve grafts (CD NG) as a control group for this study. Then, the nerve tissue was extracted with supercritical carbon dioxide. To improve the extraction efficiency, the obtained nerves were first precooled at −20 °C for 5 h and then placed in a vacuum freeze dryer (Oumeng, Shanghai, China) for 24 h (Fig. 1C). Second, the processed nerve tissue was subjected to fat extraction treatment in a supercritical carbon dioxide extraction apparatus (Joel, Dalian, China) at 30 °C and 5.5 MPa for 6 cycles, with each cycle being 45 min (Fig. 1D). Finally, the nerve tissue processed through the above steps was sterilized using γ-ray irradiation with a dose of 20 kGy cobalt 60 and then aseptically vacuum packaged (Fig. 1F). At that point, based on pure chemical decellularization technology, we obtained cell-free and fat-free nerve grafts (CD + $scCO_2$ NG) extracted by supercritical carbon dioxide as the experimental group of this study.

2.2. Histological and immunofluorescence analysis of ANXs

The two obtained kinds of ANXs (CD NG, CD + $scCO_2$ NG) were embedded in OCT embedding glue (SAKURA, Japan), and then frozen sections with a thickness of 6 μm were made using a freezing microtome (CM1900, Leica, USA) on the cross-section of the nerve. At the same time, natural porcine sciatic nerve (Natural SN) was selected as a control. After putting in PBS and degumming, hematoxylin and eosin (H&E) staining was performed according to the kit instructions (G1120, Solarbio, China). The tissue on the section was blocked in 10% goat serum (SL038, Solarbio, China) for 30 min. Laminin antibody (1:1000, L8271, Sigma–Aldrich, USA) from mice was used as the primary antibody to cover the nerve tissue and incubated overnight in the dark at 4 °C. The excess primary antibody was washed off with PBS and then incubated for 2 h with goat anti-mouse IgG H&L secondary antibody (Alexa Fluor 594, 1:200, ab150116, Abcam, USA) in the dark at 37 °C. The excess secondary antibody was washed off with PBS, and sections were incubated with DAPI (1:100, 62248, Thermo Fisher Scientific, USA) staining solution for 5 min in the dark, washed with PBS and mounted with aqueous mount (P10144, Thermo Fisher Scientific, USA). Finally, a microscope equipped with a DP71 camera (BX51, Olympus, Japan) was used to image the stained sections obtained in the above experiment.

2.3. Scanning electron microscopy (SEM) observations of ANXs

The above two kinds of ANXs and fresh porcine sciatic nerves were placed in a −20 °C freezer for 2 h, placed in a −80 °C refrigerator for 5 h, and then transferred to a vacuum freeze dryer for sublimation and drying for 24 h. Next, a blade (819, Leica, USA) was used to cut the nerve into a 3 mm sample, the sample was fixed on a metal tray with

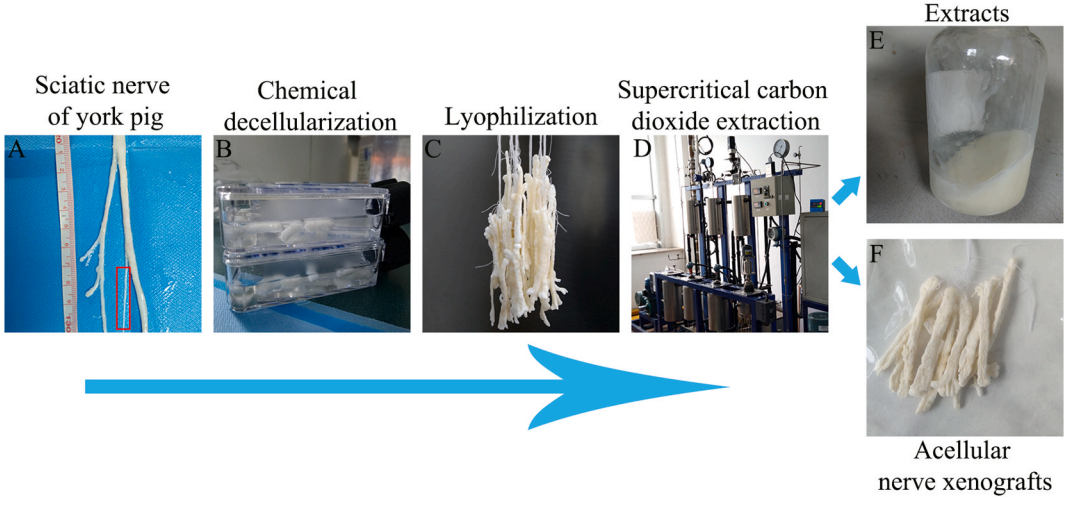

Fig. 1. The brief preparation process of ANXs based on supercritical extraction technology.

conductive glue, and then placed in an ion sputtering apparatus (Q150R, QUORUM, UK) to spray gold onto the surface of the nerve sample for 10 min. Subsequently, the metal holder carrying the nerve sample was transferred to a field emission scanning electron microscope (S4800, HITACHI, Japan) to image and record the surface and internal microstructure of the sample.

2.4. Qualitative and quantitative analysis of fat in ANXs

According to the above steps, frozen sections of two kinds of ANXs and fresh porcine sciatic nerves were obtained. To prevent the dissolution and destruction of adipose tissue, organic solvents such as acetone and xylene were prohibited during the experiment. According to the kit instructions (G1261, Solarbio, China), the sections were stained with Oil Red O to qualitatively evaluate the fat content of the nerve samples. Second, to quantitatively evaluate the fat content, we used a gas chromatography mass spectrometer (Trace1310 ISQ, Thermo Fisher Scientific, USA) to quantitatively analyze the 37 fatty acids in the nerve samples. Briefly, 30 mg of sample was dissolved in ethanol and diluted to 25 ml. One milliliter was added to a 15 ml centrifuge tube. Then, 2 ml of 5% hydrochloric acid methanol solution, 3 ml of chloroform methanol solution (volume ratio 1:1), and 100 μl of internal standard methyl octadecanoate (Sigma–Aldrich, USA) were added. The above mixture was placed in a water bath at 85 °C for 1 h. After completion, the temperature was allowed to drop to room temperature. One milliliter of *n*-hexane was added to the centrifuge tube, shaken and extracted for 2 min, and allowed to stand for 1 h. After layering, 100 μl of the supernatant was diluted to 1 ml with *n*-hexane and was tested on the machine after passing through a 0.45 μm filter membrane. Thirty-seven kinds of fatty acid mixed standard products were purchased from Sigma–Aldrich. All measurements were independently repeated three times. The following calculation formula was used to determine the content of each fatty acid in the sample:

$$Xi = \frac{Asi \times Mskli \times Fj}{Astdi \times M}$$

Xi: The content of each fatty acid in the sample (mg/kg); Asi: The peak area of fatty acid in the sample solution; Mskli: The quality of the standard product contained in the fatty acid triglyceride standard working solution drawn in the preparation of the standard measurement solution (mg); Fj: The conversion factor of each fatty acid triglyceride into fatty acid, see Supplementary Table 1; Astdi: Peak area of each fatty acid in standard test solution; M: The weight of the sample (kg).

2.5. Determination of DNA content of ANXs

With reference to the published literature [63], a Quan-IT™ picogreen™ dsDNA assay kit (P7589, Invitrogen, USA) was used to determine the DNA content of the two ANXs after decellularization and defatting. Briefly, two ANXs and natural porcine sciatic nerve samples were added to a 1.5 ml EP tube containing 500 μl of cell lysis buffer, sonicated for 15 s, and centrifuged at 1000 rpm for 5 min. The supernatant was collected, and then the fluorescence intensity was measured using a Nanodrop ND3300 spectrofluorometer (Thermo Fisher Scientific, USA) for DNA quantification. The measurement was repeated 3 times, and after reading, the measurement unit (ng/μl-ng/mg) was converted.

2.6. Western blot analysis of extracts and CD + $scCO_2$ NG

The extracts were collected during 6 cycles of supercritical extraction, and WB detection of proteins of interest together with CD + scCO2 NG was performed. Sixty milligrams of the sample was placed in a test tube, 10 times the tissue volume of the protease inhibitor was added, and the tube was placed in a homogenizer for 100 s, during which the temperature was intermittently lowered. After the end, the sample tube was removed, placed in an ice bath for 30 min, and shaken every 5 min to ensure complete lysis of the tissue. Afterward, the samples were centrifuged at 12000 g for 10 min, and the pellet was dissolved in a solution containing 0.01 M HCl and 1 mg/ml pepsin. Soluble and insoluble protein mixtures were separated by electrophoresis on a 15% sodium dodecyl sulfate-polyacrylamide gel, and then the protein was transferred to a polyvinylidene fluoride (PVDF) membrane. The membranes were blocked in 5% nonfat dry milk at 4 °C for 1 h and incubated with rabbit anti-collagen I (1:1000, ab34710, Abcam, USA), rabbit anti-collagen II (1:1000, ab34712, Abcam, USA), rabbit anti-collagen IV (1:1000, ab6586, USA) and mouse anti-fibronectin (1:1000, ab6328, Abcam, USA) primary antibodies overnight at 4 °C. Next, the membranes were incubated with secondary antibodies for 1 h at room temperature with HRP-anti-rabbit (1:500; Zhongshan, China) and HRP-anti-mouse (1:500; Zhongshan, China) antibodies. The membranes were developed using an enhanced chemiluminescence substrate (Thermo Fisher Scientific, USA). Finally, membranes were scanned using an AI 600 ultrasensitive multifunctional imager (GE, USA). All measurements were independently repeated three times.

2.7. Proteomic analysis of ANXs based on label-free quantitative technology

Two kinds of ANXs stored in a −20 °C refrigerator after sterilization were used as experimental samples, and natural SN was used as a control sample. One gram of each of the three kinds of nerve samples was placed in 3 centrifuge tubes, and then 6 mL of protein extraction buffer was added to each sample. After mixing, the samples were thoroughly ground for 10 min, sonicated at low temperature for 5 min, and centrifuged at 5500 g for 10 min. The supernatant was discarded, and the resulting precipitation was dried in a fume hood for subsequent use. A BCA kit (23225, Thermo Fisher Scientific, USA) was used to determine the protein concentration of the above samples, and the samples were separated by running a gel to observe the protein distribution. One hundred micrograms of each of the above samples were subjected to the FASP method [64] for protein enzymolysis, and high-performance liquid phase and mass spectrometry technology were used to detect and analyze the protein samples.

The international mainstream proteomics analysis software Proteome Discoverer 2.1 was used to perform protein identification and analysis of the raw data collected by LC–MS/MS. The search database was downloaded from the UniProt (https://www.UniProt.org/) website, and the search engine was Sequest HT. Differentially expressed proteins (DEPs) were screened using mapDIA software. To identify the primary functional pathways of the DEPs in three kinds of nerve samples, Gene Ontology (GO) and Kyoto Encyclopedia of Genes and Genomes (KEGG) pathway-enrichment analyses were performed using the Database for Annotation, Visualization, and Integrated Discovery (DAVID) 6.8 (https://david.ncifcrf.gov/), and the R language ggplot2 installation package was used to draw bubble charts. GO analysis consists of three categories: biological processes (BP), molecular functions (MF), and cell components (CC). The statistical threshold was set as $P < 0.05$ with fold change (FC) ≥ 1.5.

2.8. Bioactivity of SCs on the ANXs scaffold

The 3 mm nerve samples were sterilized using γ-rays produced by cobalt 60 and used as a scaffold for cell culture. Rat-derived Schwann cell lines (RSC96) were purchased from the Cell Bank of the Chinese Academy of Sciences and used in this experiment after resuscitation. The two ANXs plates were transferred to a 6-well plate in a sterile environment, with 3 replicate wells for each ANX. The cells were passaged to generation 2 (P2). After digestion and resuspension in collagenase NB4 (17454, SERVA, Germany), the cells were counted and immediately seeded into 6-well plates, and the number of seeded cells per well was 200,000. Then, Dulbecco's modified Eagle's medium/Ham's F-12 Mix

(DMEM/F-12, Corning, USA) containing 10% fetal bovine serum (FBS) (35-011-CV, Corning, USA) was added, and the 6-well plate was transferred to an incubator at 37 °C and incubated in an atmosphere of 5% CO_2. Cells were cultured to the 3rd and 7th days for live/dead cell double staining, secretion, immunofluorescence and scanning electron microscopy analysis. According to the instructions of the kit (40747ES76, Yeasen, China), alive and dead staining was performed on cells adhering to the ANXs scaffold, and then a laser confocal microscope (TCS SP8, Leica, USA) was used to capture images. Next, the cell composite scaffold was fixed in 4% paraformaldehyde (P1110, Solarbio, China) for 1 h at 4 °C and washed 3 times with PBS for 5 min each. Then, immunofluorescence staining of the cell composite scaffold was performed using S100 β (ab52642, Abcam, USA) antibody, using the relevant steps described above, and images were obtained using a confocal microscope. Finally, the cell composite scaffolds that had been cultured for 7 days were fixed in 2.5% glutaraldehyde (P1126, Solarbio, China) and dehydrated with ethanol step by step, which was the same as the previous steps, and cell morphology on the surface of the scaffold was observed by scanning electron microscopy.

The medium of the cell composite scaffold cultured to the third day was used to determine cytokine secretion from Schwann cells. In brief, the medium of each group was centrifuged at 1500 rpm and 4 °C for 10 min, the concentration of NGF and BDNF in the supernatant was assessed using ELISA kits, the rat GDNF ELISA kit (EK0363, BOSTER, China) and the rat NGF/NGFβ ELISA kit (EK0471, BOSTER, China), and the absorbance of each well at 450 nm was determined using a spectrophotometer (EPOCH TAKE 3, Bio-Tek, USA). Ten milligrams of grafts were cut using microscissors and then dissolved in 0.01 mol/l HCl pepsin (working concentration 1 mg/ml, P6887, Sigma–Aldrich, USA) for 48 h. The mass ratio of pepsin to ECM powder was 1:10, and the undissolved particles were removed by ultracentrifugation at 20000 rpm. Then, the supernatant was collected for cell experiments. Schwann cells were resuspended to a concentration of 4×10^4 cells ml^{-1}, and the cell suspension was inoculated into a 96-well plate (250 μL per well). The 96-well plate was divided into 3 groups: normal, CD NG, and CD + $scCO_2$ NG. Cell-free medium (250 μl per well) was used as a blank control. The CD NG group was cultured with complete medium containing 10% CD NG enzyme digestion supernatant, and the CD + $scCO_2$ NG group was cultured with complete medium containing 10% CD + $scCO_2$ NG enzyme digestion supernatant. As a control, the normal group was cultured in complete medium, and cell proliferation of the three groups was determine using the CCK8 kit (G4103, Servicebio, China) at 4 time points on days 1, 3, 5 and 7. Finally, the absorbance of each well at 450 nm was determined using a spectrophotometer (EPOCH TAKE 3, Bio-Tek, USA). All measurements were independently repeated three times.

2.9. Evaluation of DRG growth on the ANXs membranes

DRG isolation and culture were performed as previously described [1]. In brief, 12-h-old SD rats were sacrificed and immersed in 75% ethanol solution for sterilization. After cutting the back skin, the spine was removed, divided into two equal halves along the sagittal plane, and the DRG was removed from the bilateral intervertebral foramen under a microscope. The tissue was placed in a medium-sized culture dish on an ice bag containing complete medium with Schwann cells, and microforceps were used to carefully peel off the epineurium of DRG. DRG with the epineurium removed was inoculated into a six-well plate containing uncoated round glass coverslips (normal group) or coated with CD NG or CD + $scCO_2$ NG membranes. Circular glass slides coated with ANXs membranes were obtained by the following methods: according to the previous experimental procedure, ANXs was sliced longitudinally at a thickness of 6 μm using a cryostat, attached to the surface of a circular glass slide, and then immersed in 75% ethanol and sterile PBS for 5 min for degumming and sterilization followed by use in cellular experiments after packaging. Neurobasal A medium (10888–022, Gibco, USA) was added to each well of the six-well plate, which contained B-27 (1:50, 17504044, Gibco, USA) and GlutaMAX (1:100, 35050–061, Gibco, USA). On the 5th day of culture, immunohistochemical staining was performed to determine the growth of axons on the surface of the ANXs.

The immunohistochemistry steps were the same as before. The primary antibody was mouse anti-NF200 (1:200, N5389, Sigma–Aldrich, USA), and then an immunohistochemistry kit (KIT-9922, Maixin, China) was used to perform secondary antibody incubation and DAB color development according to the manufacturer's instructions. After immunohistochemical staining, the ANXs membrane on the round slide was stained with Oil Red O, and the relevant steps were as described above. Finally, a microscope equipped with a DP71 camera (BX51, Olympus, Japan) was used to image the stained sections obtained in the above experiment. Five fields of view were randomly selected for each group of samples, and two professional experimenters used Image-Pro Plus software (IPP 6.0, Media Cybernetics, USA) to measure the growth length, density and steering angle of DRG axons.

2.10. Animals

The 84 male Sprague–Dawley rats (age: 3 months; weight: 280–300 g) used in this study were bred in a sterile environment and were all provided by Sibeifu (Beijing, China) Biotechnology Co., Ltd. (license No. SCXK(Jing)2019–0010). The Ethics Committee of the Chinese People's Liberation Army General Hospital approved the experimental procedures related to experimental animals in June 2019 (approval number: 2019-x6-05). All procedures with experimental animals were implemented in accordance with the "Guidelines for the Care and Use of Laboratory Animals".

2.11. Evaluation of immune tolerance after subcutaneous implantation of ANXs

The previously prepared ANXs was cut into 15 mm nerve segments along the longitudinal direction, and nerve bundles with a diameter of 1–1.5 mm were separated using microforceps and microscissors for animal experiments. Similarly, natural porcine sciatic nerves of the same specification were used as positive controls, and the rat's own sciatic nerve was used as a negative control. Thirty-six SD rats were randomly divided into four groups: autogenous SN, CD NG, CD + $scCO_2$ NG, and natural SN. The rats were anesthetized by intraperitoneal injection of 3% pentobarbital sodium solution (30 mg/kg), and the back hair was removed to ensure that a 2 cm^2 square area was reserved at the connecting line between the spine and anterior superior iliac spine for the subcutaneous embedding experiment. After disinfecting the square operation area on the back, the center of the operation area carefully cut the back skin 1 cm along the sagittal position and put the corresponding graft under the skin of the rat. It should be noted that the autologous SN group had the sciatic nerve on the right side of the rat cut and then placed under the skin. To alleviate the pain in this group of rats, we transplanted hollow chitosan conduits into the nerve defects.

After hemostasis, the subcutaneous fascia layer and the skin was sutured in turn. Finally, all rats were fed under standardized laboratory conditions. Overdose anesthetics were intraperitoneally injected (50 mg/kg), and 3 rats in each group were sacrificed 1, 2 and 4 weeks after surgery. The graft and surrounding skin tissue were removed, fixed and sliced for HE and immunohistochemical staining. The specific staining steps were the same as described above, and the primary antibodies used in immunohistochemistry were as follows: rabbit anti-CD4 (1:4000, ab237722, Abcam), mouse anti-CD8 (1:200, ab33786, Abcam) and mouse anti-CD68 (1:3000, ab955, Abcam).

2.12. In vivo implantation in long-distance sciatic nerve defects in rats

The surgical procedure was performed as previously described [63]. According to the graft used to bridge the sciatic nerve defect, 48 SD rats were randomly divided into 4 groups (12 in each group): hollow

chitosan conduit (HCC), CD NG, CD + $scCO_2$ NG, and ANG. After anesthesia, the hair of the right hind limb was removed. After disinfecting the posterolateral skin of the right hind limb, the skin was incised and separated along the intermuscular space. The sciatic nerve was carefully exposed, the fat and connective tissue around the nerve were removed and separated from the muscle space. Between the proximal and distal branches of the sciatic nerve, a 15 mm nerve segment was cut and removed, and then 4 types of grafts were used to bridge the nerve defect. Under the microscope, 8/0 sutures with needles were used to suture the outer membranes of the two nerve stumps and fix them on both ends of the graft. In the ANG group, the excised rat sciatic nerve was turned over 180° to bridge the nerve defect in situ. Of note, HCC was provided by the Department of Orthopedics and Traumatology, Peking University People's Hospital, and patents were obtained from Peking University People's Hospital and China Textile Research Institute (Patent No. 01136314.2) [65]. After hemostasis, the subcutaneous fascia layer and the skin were sutured in turn. After waking up, all rats were fed under standardized laboratory conditions.

2.13. Gait analysis based on CatWalk

The experimental procedure of analyzing rat gait using the Catwalk footprint analysis system (XT 10.6, Noldus, Netherlands) was performed as previously described [1]. Briefly, the Catwalk footprint analyzer was started, and the width of the footprint recording table was adjusted according to the size and width of the experimental animal (SD rat) so that the rat could pass through without turning around. The distance between the camera and the footprint recording table was properly adjusted so that the footprints of the experimental animals could be clearly observed and recorded. The rats in each group were properly trained to adapt to the environment of the footprint analyzer. After defecation and urination, the experimental rats were placed at the beginning of the footprint recording table, and appropriate light sound or light stimulation was given to make them walk to the other end of the footprint recording table by themselves. The start and end of a single experiment were confirmed by professional operating software. At each time point of the experiment, at least 6 rats in each group walked in accordance with the analysis requirements of the software. The rats were tested and analyzed for gait 2, 4, 6, 8, 10 and 12 weeks after surgery. According to the experimental records, the Catwalk XT 10.6 system was used to calculate the SFI and the standing/swing time ratio of each rat. The following calculation formula was used to determine the sciatic nerve index (SFI):

$$SFI = 109.5(ETS-NTS)/NTS-38.3(EPL-NPL)/NPL+13.3(EIT-NIT)/NIT-8.8$$

E: The injured hindfoot of the rat; N: The normal hindfoot of the rat; TS: The toe width of the hindfoot footprint; PL: The length of hind foot print; IT: The width of the middle toe of the hind foot print.

2.14. Histological evaluation of gastrocnemius muscle

Twelve weeks after the operation, rats in each group were sacrificed by intraperitoneal injection of excessive anesthetics. The target organs (gastrocnemius) of the operative side and normal side were removed and weighed on an electronic balance to calculate the wet weight recovery rate of the gastrocnemius. The formula was X% = W(E)/W(N). In the formula, E is the operation side of the rat, N is the normal side of the rat, and W is the measured wet weight of the gastrocnemius muscle (g).

The weighed gastrocnemius muscles of each group were imaged and recorded, and then the muscle belly was cut out and placed in 4% paraformaldehyde solution for fixation for 24 h. Routine dehydration and embedding were performed, and then the automatic tissue paraffin slicer (RM2125, Leica, USA) was used to make cross-sectional 5 μm sections of muscles in each group. After conventional pathological baking, dewaxing and rehydration, Masson staining was performed according to the kit instructions (G1346, Solarbio, China) to evaluate differences in the cross-sectional area of muscle fibers in each group. Fifteen fields of view were randomly selected for each group of samples, and the average cross-sectional area of gastrocnemius muscle fibers was measured by two professional experimenters using IPP 6.0 software.

2.15. Histological evaluation of regenerated axons

Four weeks after the operation, 1 experimental rat in each group was injected with an overdose of anesthetic for euthanasia. The bridging nerve segment (graft) was removed from 6 μm longitudinal frozen sections to observe the growth of regenerated axons in each graft. The specific immunofluorescence staining steps were the same as described above. The primary antibody was mouse anti-NF200 (1:200, N5389, Sigma–Aldrich, USA), and the secondary antibody was goat anti-mouse IgG H&L (Alexa Fluor® 488, 1:200, ab150113, Abcam). Twelve weeks after the operation, all remaining experimental rats in each group were sacrificed after being injected with an overdose of anesthetic. The muscle gap along the skin suture was carefully opened, the grafts in each group were fully exposed, and images were acquired. The distal 1/5 (length: 3 mm) of the bridging nerve segment was removed, and 6 μm transverse frozen sections (5 samples per group) were obtained to qualitatively observe the quality of regenerated axons in each group. The specific immunofluorescence staining steps were the same as described above. The primary antibodies were mouse anti-NF200 (N5389, Sigma–Aldrich, USA) and rabbit anti-MBP (1:5000, ab218011, Abcam), and the secondary antibodies were goat anti-mouse IgG H&L (Alexa Fluor® 594, 1:200, ab150116, Abcam) and goat anti-rabbit IgG H&L (Alexa Fluor® 488, 1:200, ab150077, Abcam).

To further quantitatively evaluate the quality of regenerated axons in each group, the remaining nerve segments (6 samples per group) were quickly removed and placed in 2.5% glutaraldehyde for 12 h for fixation followed by 1% osmium tetroxide solution for 12 h at 4 °C. Then, the nerve segments were dehydrated in gradient ethanol and embedded in a mixture of glycolmethacrylate (GMA) mixed embedding medium and acetone in equal proportions for 72 h. The unnecessary parts around the embedded tissue block were trimmed, and the cross-section of the tissue was made into semi-thin sections with a thickness of approximately 700 nm. According to the kit instructions (1% in sodium borate, G3663, Solarbio, China), the sections were stained with toluidine blue O solution. Finally, a microscope equipped with a DP71 camera was used to acquire images of the stained sections obtained in the above experiment. Ten fields of view were randomly selected for each group of samples, and 2 professional experimenters used IPP 6.0 to measure the mean density of myelinated nerve fibers.

According to the micrographs stained with toluidine blue, the parts of interest of each group of samples were determined, and then the cross-sections of the distal sections of the nerve grafts of each group were cut into ultrathin sections at a thickness of 70 nm. The sections were transferred to a grid and then double stained with 3% uranyl acetate-lead citrate. The grid with the slides was placed under a transmission electron microscope (CM-120, PHILIPS, Netherlands) to observe and take pictures of the regions of interest. Ten fields of view were randomly selected for each group of samples, and 2 professional experimenters used IPP 6.0 to measure the mean diameter of myelinated nerve fibers and the mean thickness of the myelin sheath.

2.16. Statistical analysis

All data are expressed as the means ± SD, and there were at least three replicates. After categorizing and sorting the data, Statistical Program for Social Sciences (SPSS) software (version 22.0, IBM, USA) was used for statistical analysis. For measurement data with equal variances, Student's *t*-test was used to compare the differences between the two groups, and one-way analysis of variance (ANOVA) was used to compare the differences between multiple groups. For measurement

data with uneven variances, nonparametric tests were used to analyze the differences between groups. Count data are expressed as frequencies or rates, and the χ^2 test was used to analyze differences between groups. $P < 0.05$ indicates that the difference between groups is statistically significant.

3. Results

3.1. Characterization of ANXs

After a series of treatment procedures (Fig. 1), including chemical washing (Fig. 1B) and supercritical carbon dioxide extraction (Fig. 1D), we obtained the final acellular nerve xenografts (CD + $scCO_2$ NG) (Fig. 1F). Purely chemically decellularized nerve xenografts (CD NG) (Fig. 1C) served as the control group in this experiment. Second, after processing using the supercritical carbon dioxide extractor, paste-like extracts (Fig. 1E) were collected and used for subsequent analysis. Of note, the ANXs derived from adult Yorkshire pigs is too thick compared to the rat sciatic nerve. Therefore, we selected only one bundle of nerves (Fig. 1A) for subsequent in vivo experiments in rats in this study.

Next, we performed a series of analyses on the general characteristics of the two kinds of ANXs using laboratory-related techniques (Fig. 2A). To more precisely determine the effect of the experimental treatment, we chose the Natural SN as a reference. Immunofluorescence staining revealed that after chemical washing and supercritical extraction treatment, laminin, an important component of the neural basement membrane, was retained to a large extent. At the same time, DAPI staining demonstrated that the nucleus was largely removed (Fig. 2B). HE staining also showed similar results. Blue-stained nuclear components were not observed in ANXs, while extracellular matrix components were retained. Importantly, we still observed a porous nerve basement membrane tube inside the CD + $scCO_2$ NG (Fig. 2C). SEM showed that compared to the tightly arranged nerve fibers of naive nerves, the graft contained a three-dimensional oriented structure of well-preserved nerve fibers and nerve basement membrane tube (Fig. 2C).

3.2. Evaluation of defatting and decellularization

To qualitatively evaluate defatting of the two grafts, we stained the three nerve samples with Oil Red O. The results showed that the red-stained fat was primarily localized around the nerve bundles of the natural SN. The degree of fat removal by simple chemical washing (CD NG) was very limited, but the red-stained fat was almost invisible after supercritical extraction treatment (CD + $scCO_2$ NG) (Fig. 3A). In addition, we quantitatively evaluated the defatting and decellularization of ANXs.

First, we performed chromatogram analysis of 37 fatty acids in three nerve samples, and each peak represents one of the fatty acids (Fig. 3B–D). After calculating the peak area and performing conversion, the fat content of the nerve sample was obtained. After 6 cycles of supercritical carbon dioxide extraction, the fat content of nerve samples gradually decreased. Among them, the fat content of natural SN was 635259.85 ± 17388.23 mg/kg, and the fat content of ANX (CD + $scCO_2$ NG) after extraction was 257597.81 ± 18482.19 mg/kg (Fig. 3E). At the same time, we performed fat quantification on nerve samples treated with pure chemical washing (CD NG: 594168.16 ± 15735.26 mg/kg). As shown in Fig. 3F, there was no significant difference between the Natural SN and CD NG groups ($p = 0.101$), but there was a significant difference between the CD NG and CD + $scCO_2$ NG groups ($p < 0.001$). In addition, we quantified the 19 fatty acids with the highest content among the 37 fatty acids in the two kinds of ANXs. The data are expressed as the percent decrease in the content of a single fatty acid compared to natural SN. There were significant differences in the contents of 19 fatty acids between the two kinds of ANXs ($p < 0.01$) (Fig. 3G and Supplementary Table 2). Analysis of the DNA content of the nerve

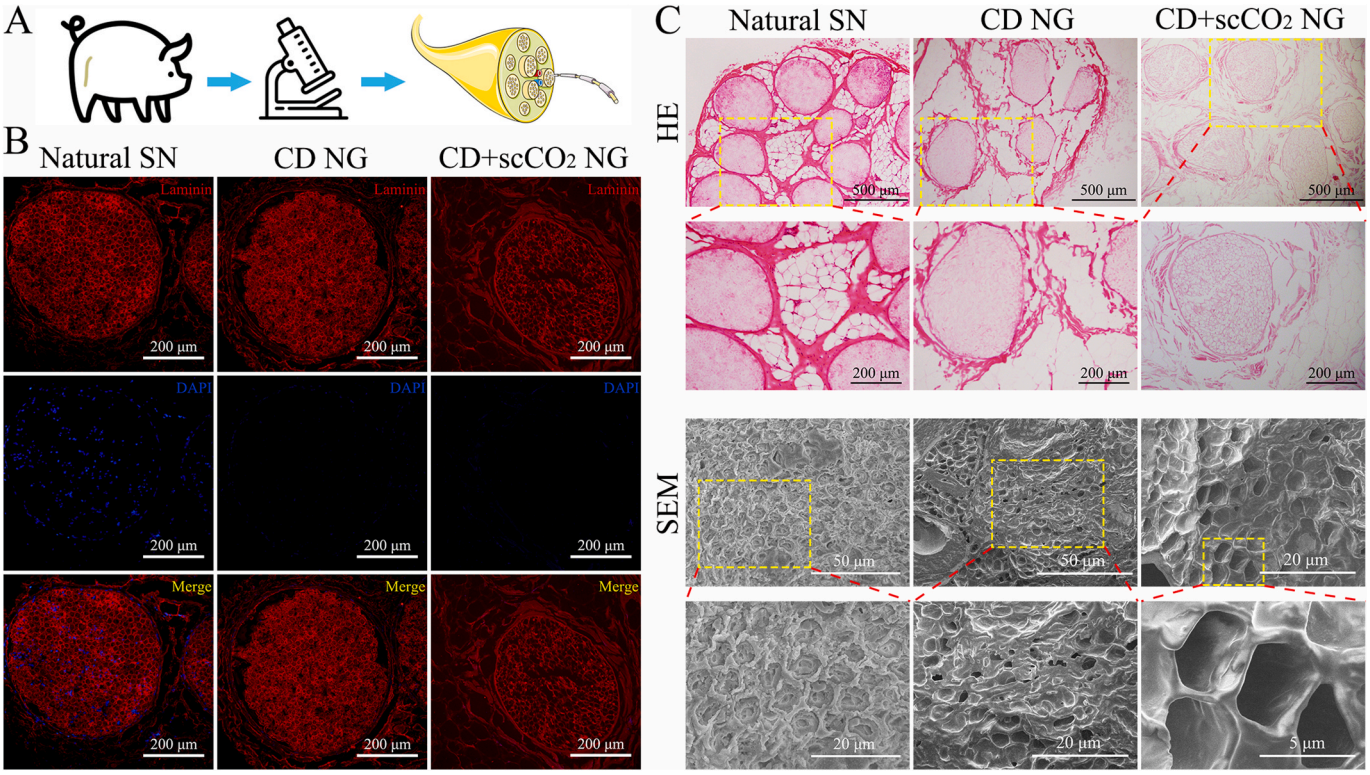

Fig. 2. The general characteristic of ANXs. (A) Schematic diagram of the experimental analysis of ANXs and Natural SN obtained from Yorkshire pigs. (B) Immunofluorescence detection of the main components of neural basement membrane tubes in ANXs and Natural SN. (Laminin: red, nucleus: blue). (C) HE staining and scanning electron microscopy (SEM) images of ANXs and Natural SN. (The picture below is an enlarged view of the yellow area in the picture above).

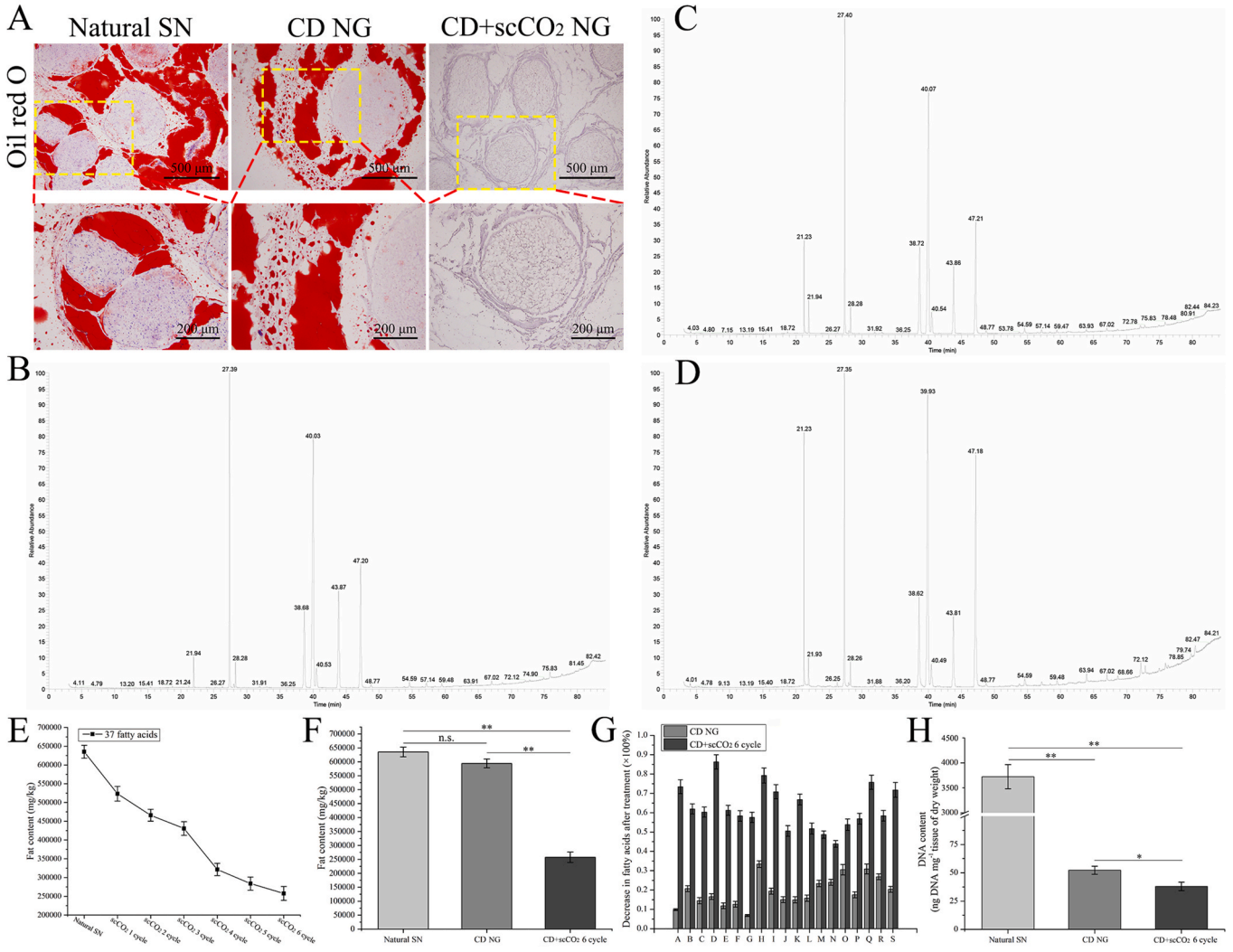

Fig. 3. Analysis of the defatting effect and DNA content of ANXs. (A) Oil red O staining of ANXs and Natural SN (the picture below is an enlarged view of the yellow area in the picture above). (B, C, D) Chromatogram analysis of 37 fatty acids of the natural SN, CD NG and CD + $scCO_2$ NG (each peak represents one of the fatty acids). (E) The relationship between fat content and extraction cycle. (F) The fat content of ANXs and Natural SN. Data are presented as the mean ± SD (n = 3). (G) The percent decrease of 19 fatty acids with the highest content among the 37 fatty acids in the two kinds of ANXs. Data are presented as the mean ± SD (n = 3). (H) DNA content of ANXs and Natural SN. Data are presented as the mean ± SD (n = 5). Statistical analysis: n.s. no significances, **p < 0.01, *p < 0.05. (For interpretation of the references to color in this figure legend, the reader is referred to the Web version of this article.)

samples is shown in Fig. 3H. The DNA content of naive nerves was relatively high (natural SN: 3725.73 ± 242.31 ng/mg), the content decreased significantly after chemical washing (CD NG: 52.28 ± 3.58 ng/mg, *vs.* natural SN: $p < 0.001$), and the content further decreased after supercritical carbon dioxide extraction again (CD + $scCO_2$ NG: 38.02 ± 3.72 ng/mg, *vs.* CD NG: $p = 0.026$).

3.3. Difference in the protein composition between extracts and ANXs

To analyze the composition of the extract, we conducted WB (Fig. 4A). Considering the primary components of the neural ECM and the proteins that play a role in nerve regeneration, we tested for expression of 4 proteins (collagen I, II, Ⅳ and fibronectin) in the extracts and grafts. As shown in Fig. 4E, relative to the higher protein expression of ANXs (CD + $scCO_2$ NG), the extract contained a certain amount of collagen Ⅳ (Extracts *vs.* CD + $scCO_2$ NG: 2.52 ± 0.13 *vs.* 4.22 ± 0.26, $p = 0.0005$), while containing a small amount of collagen II (0.78 ± 0.06 *vs.* 4.5 ± 0.32, $p < 0.001$) and fibronectin (0.8 ± 0.08 *vs.* 4.03 ± 0.19, $p < 0.001$), and a trace amount of type I collagen (0.05 ± 0.01 *vs.* 4.19 ± 0.22, $p < 0.001$).

3.4. Protein quantification and proteomic analysis of ANXs

Nonlabeled (label-free) protein quantification technology is a mass spectrometry analysis of peptides produced by protein enzymatic digestion through liquid-mass spectrometry technology, comparing the signal intensities of corresponding peptides in different samples to relatively quantify the proteins corresponding to the peptides. At the same time, it has the advantages of a short experimental period, wide application range and low cost. The proteins of each group were separated by SDS–PAGE (Fig. 4B). The protein types of natural SN were the most abundant, and the protein types of ANXs were relatively reduced, primarily those with a molecular weight of less than 30 kDa. Then, we performed protein quantitative analysis on each group of samples. Cluster heatmap analysis showed that there were a large number of highly expressed proteins in the natural SN, and most of these proteins were downregulated in both kinds of ANXs (Fig. 4C). At the same time, the violin plot of protein relative abundance shows that Natural SN has a higher relative protein abundance than ANXs. The violin plot is a supplement to the protein data of the cluster heatmap (Fig. 4D).

In addition, we performed functional enrichment analysis on the

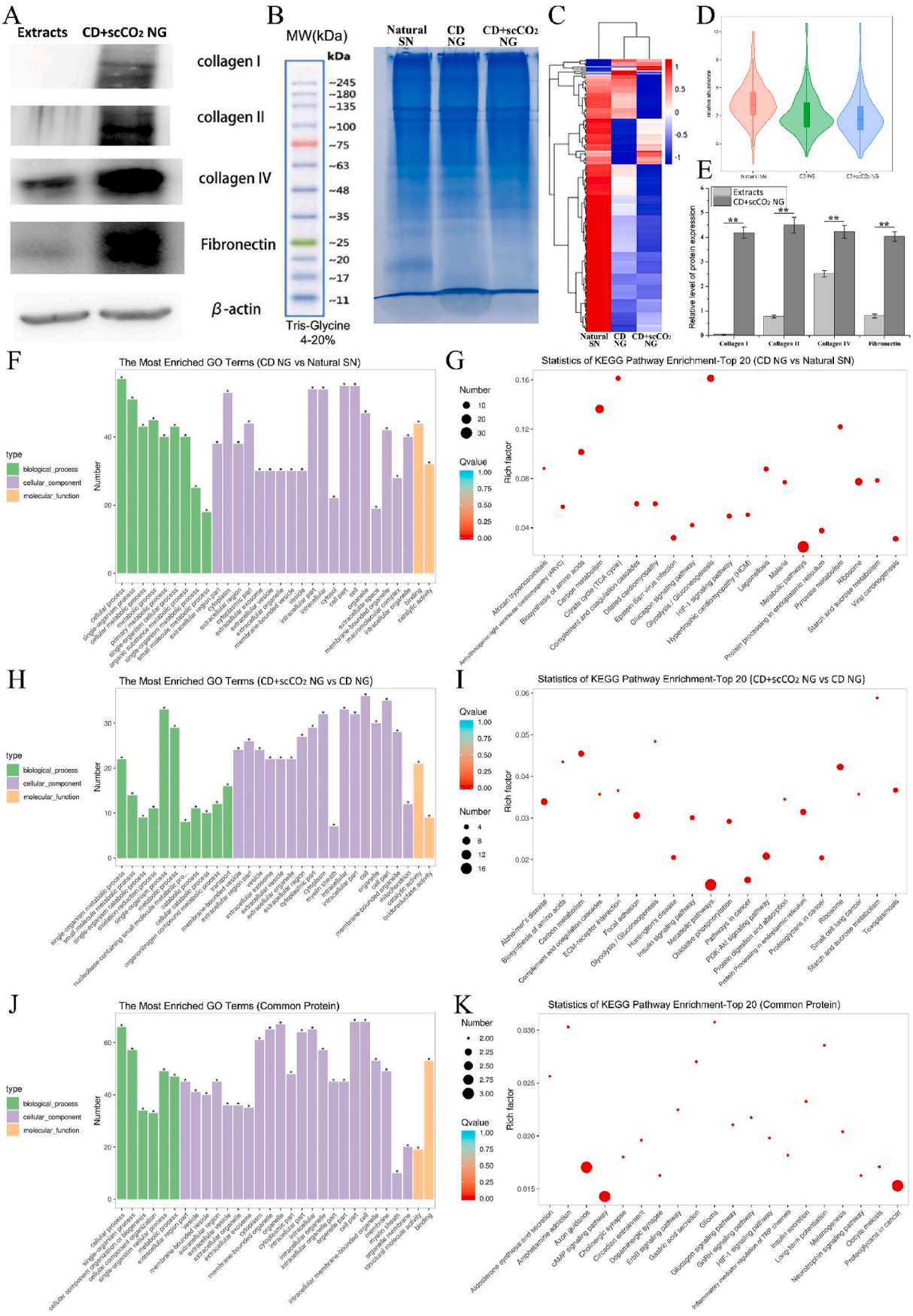

(caption on next page)

Fig. 4. Western blot and proteomics analyses of ANXs and extracts. (A) WB analysis of the expression levels of collagen I, II, Ⅳ and fibronectin in the CD + $scCO_2$ NG and extracts (the internal control was β-actin). (B) Total protein expression in ANXs and Natural SN. (C) Heatmap shows up- and downregulated proteins in ANXs and Natural SN. Red and blue represent the up- and downregulated proteins, respectively. (D) Violin chart shows the relative protein abundance in ANXs and Natural SN. (E) Quantitative analysis of the expression levels of collagen I, II, Ⅳ and fibronectin in the CD + $scCO_2$ NG and extracts. Data are presented as the mean ± SD (n = 3). (F) The most enriched GO terms of DEPs between CD NG and Natural SN based on biological process, cellular component and molecular function. (G) Statistics of the top 20 enriched DEPs in the KEGG pathway between the CD NG and natural SN are shown in the bubble plot. The abscissa KEGG term represents the name of the pathway to which the protein is enriched. The ordinate rich factor represents the enrichment factor, that is, the ratio of the protein that is enriched in the pathway of the DEPs to the ratio of the background protein that is enriched in the pathway. The larger the rich factor is, the higher the degree of enrichment. The circle size indicates the number of proteins enriched by the KEGG pathway. The circle color – Q value, represents the p-value after multiple hypothesis testing and correction. The range of Q value is [0,1]. The closer the Q value is to 0, the more significant the enrichment. (H) The most enriched GO terms of DEPs between CD + $scCO_2$ NG and CD NG based on biological process, cellular component and molecular function. (I) Statistics of the top 20 enriched DEPs in the KEGG pathway between the CD + $scCO_2$ NG and CD NG are shown in the bubble plot. The specific information of the picture is the same as above. (J) The most enriched GO terms of the common proteins of the three nerve samples based on biological process, cellular component and molecular function. (K) Statistics of KEGG pathway enrichment. The top 20 common proteins of the three nerve samples are shown in the bubble plot. The specific information of the picture is the same as above. Statistical analysis: n.s. no significances, **p < 0.01, *p < 0.05. (For interpretation of the references to color in this figure legend, the reader is referred to the Web version of this article.)

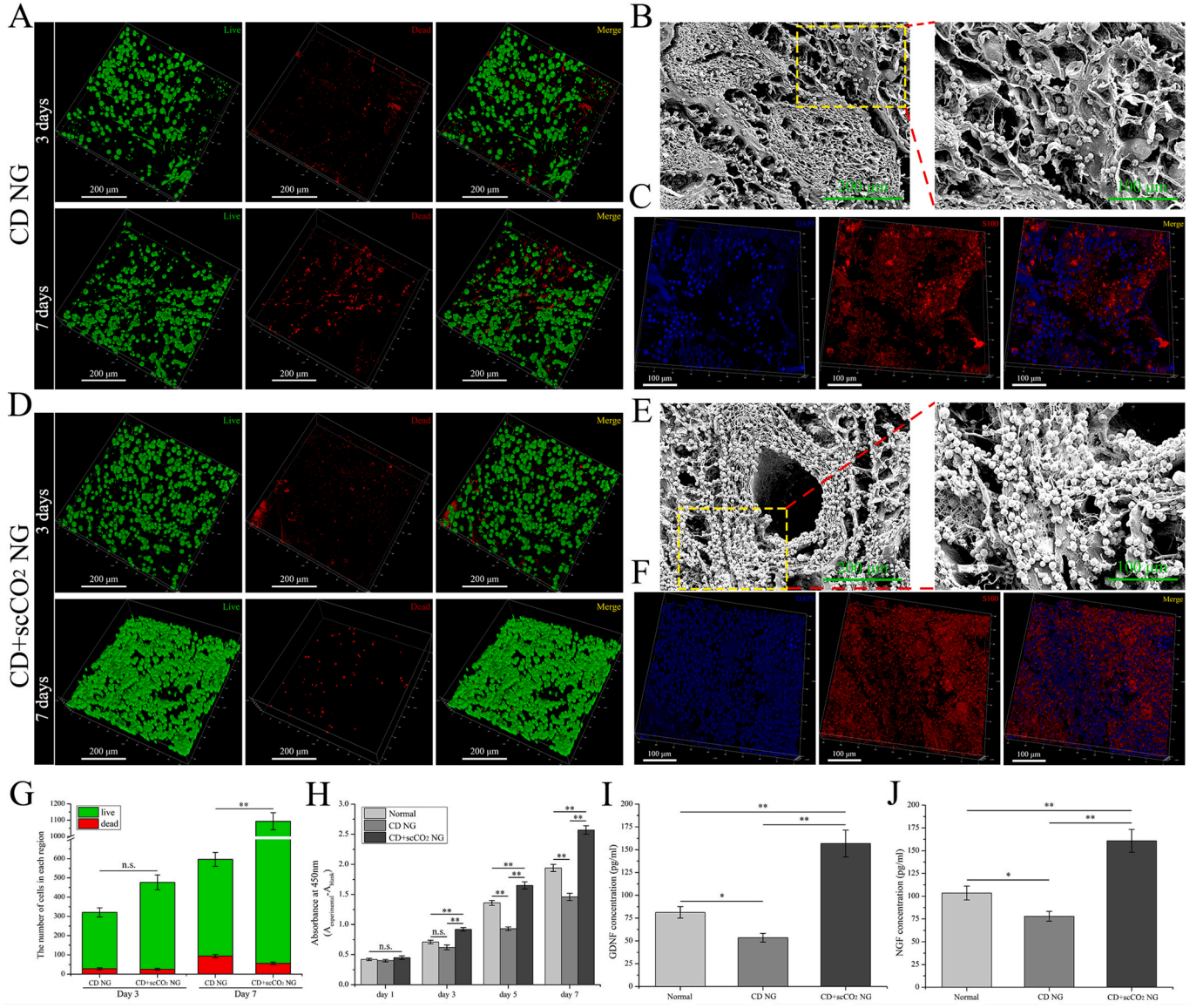

Fig. 5. Evaluation of the cytotoxicity of the ANXs scaffold in vitro. (A, D) Living/dead double staining of Schwann cells grown on the ANXs scaffold for 3 days and 7 days (live: green, dead: red). (B, E) SEM images of Schwann cells growing on CD SD and CD + $scCO_2$ NG scaffolds for 7 days (the picture on the right is an enlarged view of the yellow area in the picture on the left). (C, F) Immunofluorescence images of Schwann cells growing on CD SD and CD + $scCO_2$ NG scaffolds for 7 days, respectively (S100: red, nucleus: blue). (G) Quantification of the number of live/dead double-stained Schwann cells in each region (0.36 mm^2). Data are presented as the mean ± SD (n = 3). (H) The CCK-8 assay was performed after 1, 3, 5 and 7 days of cell culture. Data are presented as the mean ± SD (n = 5). (I, J) Quantitative analysis of the GDNF and NGF expression levels of Schwann cells on the ANXs scaffold. Data are presented as the mean ± SD (n = 5). Statistical analysis: n.s. no significances, **p < 0.01, *p < 0.05.

DEPs between the groups. Specifically, the DEPs between CD NG and Natural SN were primarily related to cellular process, single-organism process, metabolic process, and single-organism cellular process in BP. In terms of CC, it was primarily related to cell, cell part, intracellular, intracellular part and cytoplasm. In terms of MF, it was primarily related to binding and catalytic activity (Fig. 4F). In terms of the KEGG pathway, it was primarily related to metabolic pathways, carbon metabolism, glycolysis/gluconeogenesis and ribosome (Fig. 4G). Specifically, the DEPs between the CD + $scCO_2$ NG and CD NG were mainly related to the single-organism process, metabolic process, single-organism metabolic process and transport in BP. In terms of CC, differences were mainly related to cell, cell part, intracellular, intracellular part and cytoplasm. In terms of MF, they were mainly related to catalytic activity and oxidoreductase activity (Fig. 4H). In terms of KEGG pathway, differences were mainly related to metabolic pathways, carbon metabolism, focal adhesion, pathways in cancer, PI3K-Akt signaling pathway and ribosome (Fig. 4I). The common protein among the three nerve samples was the protein retained in CD + $scCO_2$ NG after repeated freezing and thawing, washing with chemical reagents and supercritical carbon dioxide extraction by Natural SN, which was primarily related to cellular process, single-organism process, metabolic process and single-organism cellular process in BP. In terms of CC, it was mainly related to organelle, membrane-bounded organelle, cell, cell part and extracellular region. In terms of MF, it was mainly related to binding and structural molecule activity (Fig. 4J). In terms of KEGG pathway, it was mainly related to Axon guidance, cAMP signaling pathway and Proteoglycans in cancer (Fig. 4K).

3.5. Cytotoxicity of the ANXs

To examine the cytotoxicity of the ANXs scaffold in vitro, we inoculated Schwann cells on the scaffold and conducted a series of evaluations. First, we stained the cells seeded on the scaffold with the living/dead cell double staining kit. A considerable number of cells adhered to the two scaffolds, indicating that this ANXs scaffold can support the attachment of Schwann cells, grow and produce ECM around them (Fig. 5A and D). Chi-square analysis of the 3-day staining results showed that there was no difference in the number of dead and alive cells between the two ANXs scaffolds (CD NG: live#292.5 ± 23.4, dead#28.2 ± 4.3; CD + $scCO_2$ NG: live#451.6 ± 38.2, dead#25.3 ± 3.6, χ^2 = 3.767, p = 0.052) (Fig. 5G). As the time was extended to 7 days, the number of cells on both scaffolds increased to a certain extent. In particular, the number of cells on the CD + $scCO_2$ NG scaffold increased significantly, while the number of red-stained dead cells on the CD NG scaffold was greater. Chi-square analysis revealed that there were significant differences in the number of dead and alive cells between the two graft scaffolds (CD NG: live#502.8 ± 36.1, dead#93.6 ± 6.9; CD + $scCO_2$ NG: live#1037.2 ± 52.5, dead#56.1 ± 5.4, χ^2 = 52.84, p < 0.001).

Second, we identified the key marker S100 in Schwann cells. The results of immunofluorescence staining showed that Schwann cells were scattered on the scaffold, exhibiting a similar distribution trend for both dead and live staining (Fig. 5C and F). In addition, to determine the growth status of Schwann cells on the scaffold more clearly, we performed scanning electron microscopic observations on the cell composite scaffolds cultured for 7 days. Similar to the results of dead and live staining, the cells on the CD NG scaffold were sparsely distributed, while cells on the CD + $scCO_2$ NG scaffold were densely distributed, and secretions could be seen between the cells (Fig. 5B and E).

Finally, we performed a quantitative assessment of cell proliferation based on CCK-8-based OD detection. With the passage of time, the number of cells in each group increased to a certain extent. One day 1, there was no difference in the number of cells in any group (Normal: 0.42 ± 0.02; CD NG: 0.4 ± 0.02; CD + $scCO_2$ NG: 0.45 ± 0.03; p = 0.105). On day 3, the number of cells in the normal group was higher than that in the CD NG group, but there was no significant difference (Normal: 0.71 ± 0.03; CD NG: 0.62 ± 0.04; p = 0.051), while the number of cells in the CD + $scCO_2$ NG group was higher than that in the CD NG group with a significant difference (CD + $scCO_2$ NG: 0.92 ± 0.03 *vs.* CD NG, p < 0.001). On days 5 (Normal: 1.36 ± 0.04; CD NG: 0.93 ± 0.03; CD + $scCO_2$ NG: 1.65 ± 0.06) and 7 (Normal: 1.94 ± 0.06; CD NG: 1.46 ± 0.06; CD + $scCO_2$ NG: 2.57 ± 0.07) and thereafter, the three groups of cells maintained a similar proliferation trend, and there were significant differences between any two groups (p < 0.01). In addition, we performed statistics on the secretion of cells on the scaffold. For the cytokine GDNF, expression levels in the normal group were higher than in the CD NG group (Normal: 81.28 ± 6.29 pg/ml; CD NG: 53.52 ± 4.82 pg/ml; p = 0.037) but lower than that in the CD + $scCO_2$ NG group (CD + $scCO_2$ NG: 156.73 ± 14.72 pg/ml *vs.* Normal, p < 0.001). Similarly, for the cytokine NGF, expression in the CD NG group was also the lowest (Normal: 103.47 ± 7.62 pg/ml; CD NG: 77.96 ± 5.37 pg/ml; CD + $scCO_2$ NG: 160.81 ± 12.54), and there were significant differences between any two groups (Normal *vs.* CD NG: p = 0.04; Normal *vs.* CD + $scCO_2$ NG: p = 0.001).

3.6. The effect of ANXs on the outgrowth of DRG neurite

To evaluate the effect of ANXs on the axons, we inoculated DRGs in (inside) and around (outside) the ANXs membrane (Fig. 6A and B). At the same time, DRGs inoculated on glass plates served as a control. As shown in Fig. 6C (left), the axons of the DRG in the control group were evenly distributed in a radial pattern. For a more detailed evaluation, we took the center of the DRG cell cluster as the origin and divided the axon region of the DRG into 8 regions, each with a 45° angle. At the same time, to observe the growth of DRG axons more clearly, we performed immunohistochemical staining (NF200) (Fig. 6C, right). For the DRGs inoculated on the outside of the ANXs membrane, we defined the area in contact with the ANXs membrane with axons as the front area, as shown in the small angle area I between the two red dashed lines in Fig. 6D (left). Correspondingly, the large-angle area II between the two red dashed lines is defined as the back area. In addition, we measured the exact steering angle of the steering nerve axon in the front area, as shown in the area in the green dashed box in Fig. 6D (left), and Fig. 6D (right) shows a partial enlargement of the corresponding area.

First, we measured the axon length of DRG. For DRGs inoculated outside the ANXs membrane (Fig. 6E, left), the mean axon length of the CD + $scCO_2$ NG group was the shortest (1142.82 ± 213.55 μm), and the mean axon length of the normal group was the longest (1264.52 ± 181.74 μm), but there was no significant difference among the three groups (CD NG: 1199.46 ± 250.39 μm, p = 0.683). For DRGs inoculated inside the ANXs membrane (Fig. 6E, right), the mean axon length of the CD + $scCO_2$ NG group was the longest (1737.19 ± 261.82 μm), and the mean axon length of the normal group was the shortest (1264.52 ± 181.74 μm). There was no significant difference between the normal and CD NG groups (CD NG: 1350.5 ± 201.82 μm, p = 0.456). However, there were significant differences between the CD + $scCO_2$ NG and the CD NG groups (p = 0.0168).

As shown in Fig. 6A (top), for the DRG inoculated on the outside of the CD NG membrane, it was difficult for its axons to enter red-stained adipose zones 1 and 3 (green number label). At the same time, the axons in interadipose zone 2 (green dotted line callout) extended for a longer distance and rarely entered adipose zones 1 and 3. A small number of axons entering adipose zone 3 exhibited disorderly growth and a certain tendency of degeneration. For DRGs inoculated inside the CD NG membrane (Fig. 6A, bottom), the axon growth range was primarily in nonadipose zones 4 and 5, while axons were rarely observed in red-stained adipose zones 1, 2, 3, or 6. In addition, we observed that axons located in adipose zone 3 and nonadipose zone 4 displayed a significant turn (green solid arrow). In the gap of adipose zone 6, only one axon entered the nonadipose zone after passing through.

As shown in Fig. 6B (top), for DRGs inoculated on the outside of the CD + $scCO_2$ NG membrane, compared to the CD NG group, axons of the

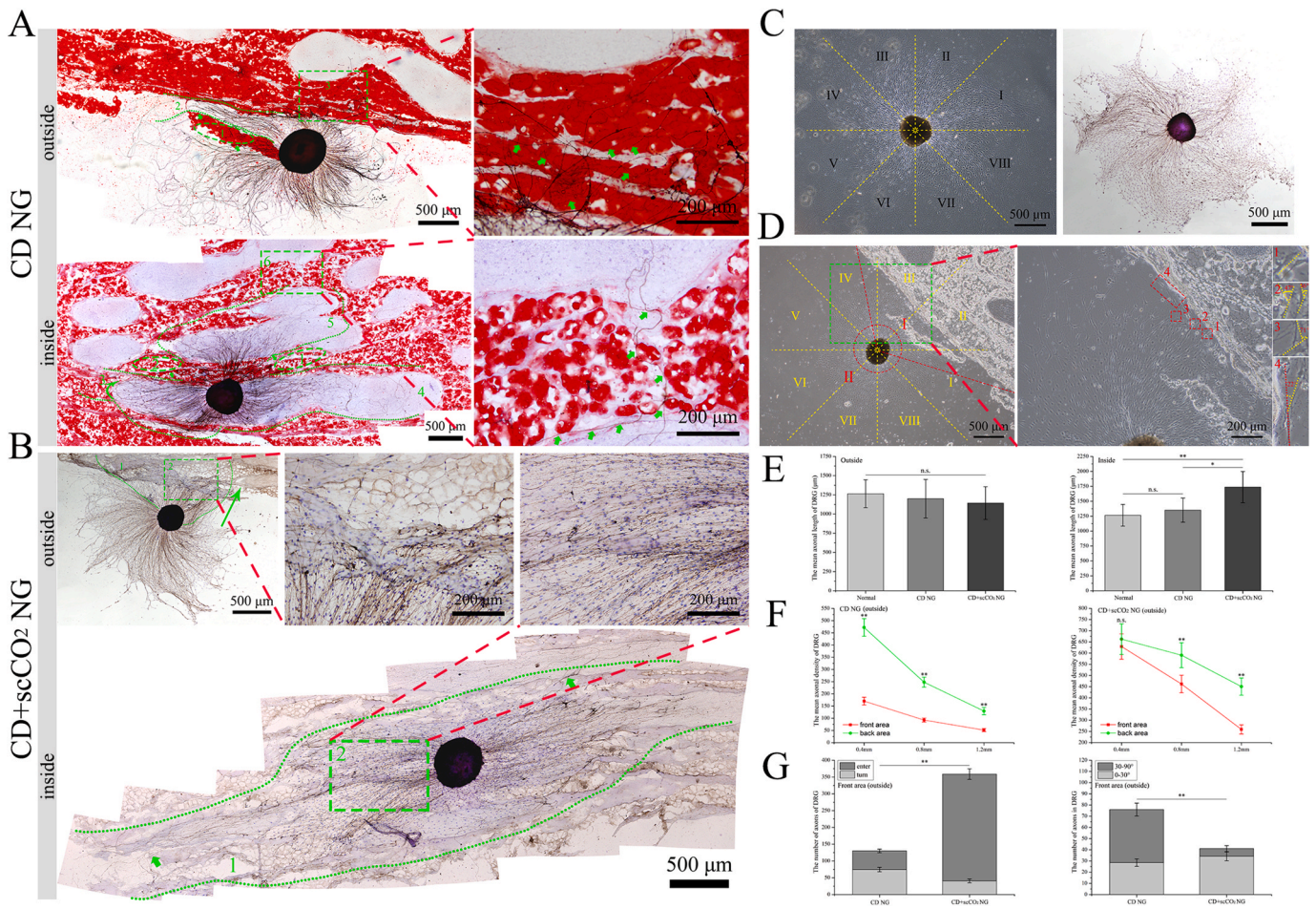

Fig. 6. Axonal outgrowth of DRGs on the ANXs membrane. (A) Axonal outgrowth of DRGs in (inside) and around (outside) the CD NG membrane. In the picture on the upper left corner, areas 1 and 3 are adipose zones, area 2 marked by the green dashed line is the interadipose zone, and green arrows indicate degenerative and turning axons; The picture on the upper right corner is an enlarged view of the area 3 in the picture on the upper left corner, and green arrows indicate degenerative and turning axons. In the picture on the bottom left corner, areas 1, 2, 3 and 6 are adipose zones, area 4 and 5 marked by the green dashed line is the nonadipose zones, and green arrows indicate turning axons. The picture on the bottom right corner is an enlarged view of the area 6 in the picture on the bottom left corner, and green arrows indicate turning axons entering the nonadipose zone after passing through. (B) Axonal outgrowth of DRGs in (inside) and around (outside) the CD + $scCO_2$ NG membrane. In the picture on the upper left corner, area 1 represents axons entering the CD + $scCO_2$ NG membrane, and the green arrow indicates the approximate growth direction of axons in area 2. The picture on the right is an enlarged view of area 2 in the picture on the upper left corner. In the picture on the bottom, area 1 marked by the green dashed line represents the growth range of DRG axons inside the CD + $scCO_2$ NG membrane, and green arrows indicate axons that extend a long distance and grow well. The picture on the upper right corner is an enlarged view of area 2 in the picture on the bottom, which indicates that axons can extend inside the CD + $scCO_2$ NG membrane indiscriminately. (C) The picture on the left is the growth status of DRG in control group, the axon region of the DRG is divided into 8 regions, each with a 45-degree angle. The picture on the right is the immunohistochemical images of DRG in control group. (D) The growth status of DRGs inoculated on the outside of the ANXs membrane (the small angle area I between the two red dashed lines represents the front area in contact with the ANXs membrane with axons, and the large-angle area II between the two red dashed lines is defined as the back area). The picture on the right shows the exact steering angle of the steering nerve axon in the front area, which is an enlarged view of the yellow area in the picture on the left. (E) The mean axonal length of the DRG in (inside) and around (outside) the ANXs membrane. Data are presented as the mean ± SD (n = 3 randomly selected DRGs per group). (F) The mean axonal density at different distances (0.4 mm, 0.8 mm and 1.2 mm) from the center of the DRG inoculated on the outside of the ANXs membrane. Data are presented as the mean ± SD (n = 3 randomly selected DRGs per group). (G) The mean number of axons turned (with different steering angles) and entered the ANXs membrane in the front area. Data are presented as the mean ± SD (n = 3 randomly selected DRGs per group). Statistical analysis: n.s. no significances, **$p < 0.01$, *$p < 0.05$. (For interpretation of the references to color in this figure legend, the reader is referred to the Web version of this article.)

DRGs more easily entered the CD + $scCO_2$ NG membrane and in larger numbers. Second, for DRGs seeded inside the CD + $scCO_2$ NG membrane (Fig. 6B, bottom), their axons grew along the ECM orientation structure inside the CD + $scCO_2$ NG membrane and extended a longer distance. Importantly, the axons extended inside the CD + $scCO_2$ NG membrane indiscriminately, including the nonadipose zone and the adipose zone before extraction treatment (currently the nonadipose zone) (green arrow and green rectangular area 2).

Second, for DRGs seeded on the outside of the ANXs membrane, we quantified the density of nerve axons at different distances (0.4 mm, 0.8 mm and 1.2 mm) from the center of the DRG cell cluster (Fig. 6F). Whether in the front area or the back area, the further the distance from the DRG cell cluster, the lower the density of axons. At 0.4 mm from the DRG cell cluster, the axon just touched the ANXs membrane. The axon density of the CD NG group was significantly different in this area (front area: 170.33 ± 15.69, back area: 472.19 ± 36.15, $p < 0.001$). However, the axon density of the CD + $scCO_2$ NG group was not significantly different in this area (front area: 629.44 ± 56.75, back area: 662.64 ± 68.27, $p = 0.4271$). At 0.8 mm (CD NG-front aera: 92.71 ± 8.47, CD NG-back aera: 247.95 ± 20.62; CD + $scCO_2$ NG-front aera: 461.93 ± 39.21, CD + $scCO_2$ NG-back aera: 590.72 ± 55.62) and 1.2 mm (CD NG-front aera: 51.75 ± 6.33, CD NG-back aera: 129.36 ± 14.94; CD + $scCO_2$

NG-front aera: 258.88 ± 20.49, CD + $scCO_2$ NG-back aera: 450.56 ± 38.48) from the DRG cell cluster, the axon density of the two ANXs was significantly different in this area ($p < 0.01$).

Finally, for DRGs inoculated on the outside of the ANXs membrane, we quantified the number of axons that turned and entered the ANXs membrane in the front area (Fig. 6G, left). In the CD NG group, the number of turned axons (74.67 ± 6.21) was greater than that of entered axons (55.38 ± 5.34), while the CD + $scCO_2$ NG group exhibited the opposite result (turned: 40.72 ± 5.33, entered: 318.1 ± 15.87), and there were significant differences between the two groups ($\chi^2 = 112.93$, $p < 0.001$). Then, we measured the steering angle of the turned axon. For the convenience of statistics, we divided the turned axons into two categories with a 30° boundary (small steering angle: 0°–30°, large steering angle: 30°–90°) (Fig. 6G, right). For the CD NG group, the number of axons with large steering angles (47.36 ± 5.74) was greater than that with small steering angles (28.55 ± 3.22), while the CD + $scCO_2$ NG group showed the opposite result (0°–30°: 34.17 ± 3.79, 30°–90°: 6.92 ± 2.62), and there were significant differences between the two groups ($\chi^2 = 21.48$, $p < 0.001$).

3.7. In vivo immune response to ANXs

To evaluate host immune rejection response to ANXs, we implanted two types of ANXs under the skin of rats. After being removed at 3 time points after the operation (1, 2 and 4 weeks), HE and immunohistochemical staining were performed. In addition, to increase the contrast, we implanted the rat's autologous sciatic nerve (Autogenous SN) and the natural porcine sciatic nerve (Natural SN) under the skin of the rat and considered them negative and a positive control group, respectively. According to the results of HE staining (Fig. 7A), in the autogenous SN group (negative control), complete neurological morphology was observed at all three time points, and there was no macroscopic neutrophil accumulation in or around the autogenous SN. However, in the Natural SN group (positive control), a large number of neutrophils gathered around and inside the Natural SN at all three time points, especially at 2 weeks. For the CD NG group, a moderate number of neutrophils were observed at the interface between the host tissue and the graft implantation 1 week after the operation. Two and 4 weeks after surgery, neutrophils primarily gathered in the adipose zone between the nerve bundles. In the CD + $scCO_2$ NG group, a small number of neutrophils were seen at the interface between the host tissue and the graft implantation 1 week after the operation. Two and 4 weeks after surgery, there were almost no visible neutrophils around or inside the graft.

Combining the results of HE staining in this experiment and previously published studies [66,67], 4 weeks after implantation is considered a suitable time point for assessing the immune response. To further evaluate host immune rejection, we performed immunohistochemical staining of CD4 (the primary marker of helper T lymphocytes), CD8 (the primary marker of cytotoxic T lymphocytes) and CD68 (the main hallmark of macrophages) on the grafts in each group at 4 weeks after surgery (Fig. 7B). For the Autogenous SN group, $CD4^+$ T cells and $CD68^+$ macrophages were not detected, and only a very small number of $CD8^+$ T cells were detected. In sharp contrast, in the Natural SN group, a large number of $CD8^+$ T cells and $CD68^+$ macrophages were detected, as well

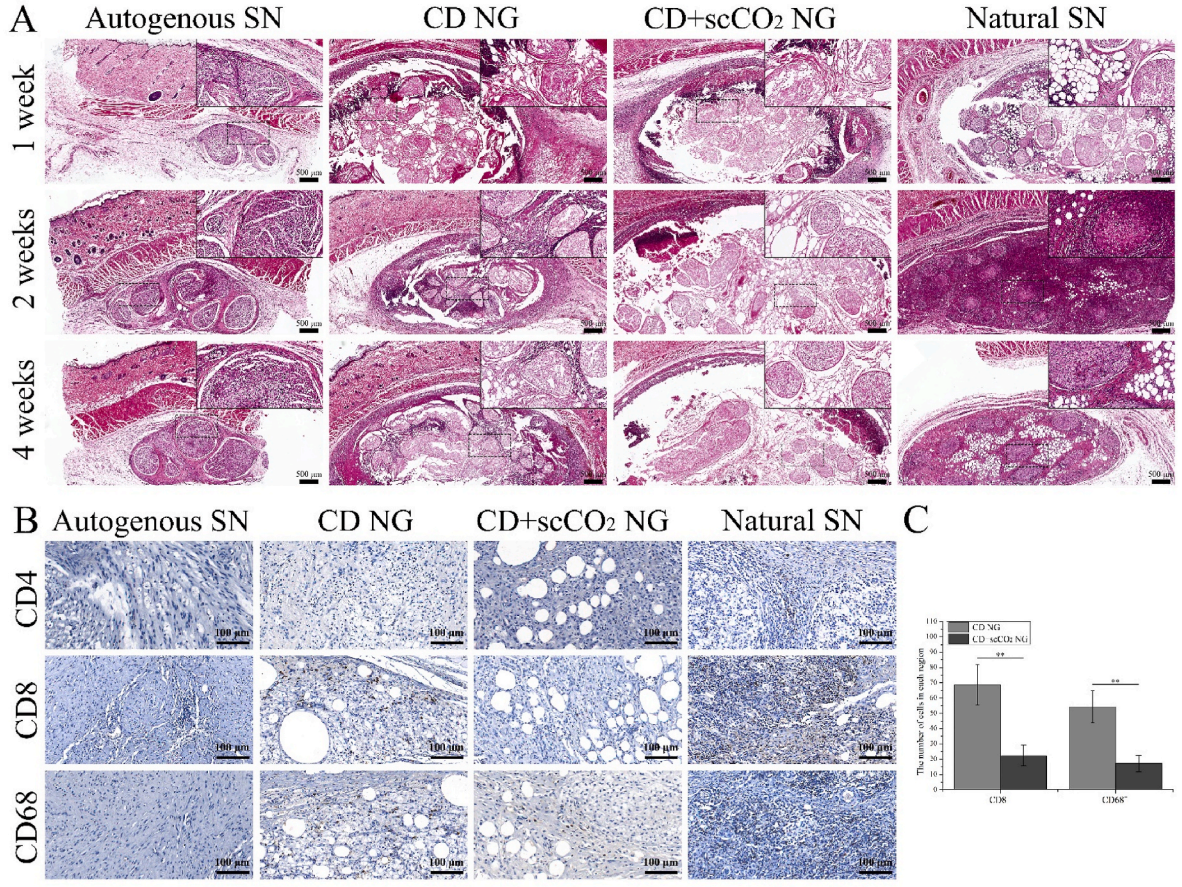

Fig. 7. Evaluation of the host immune response to ANXs subcutaneous transplantation. (A) HE staining of ANXs implanted subcutaneously in rats for 1, 2 and 4 weeks. Rat autologous sciatic nerve (autologous SN) and natural porcine sciatic nerve (natural SN) were used as the negative control group and positive control group, respectively. (B) Immunohistochemical staining (CD4, CD8 and CD68) of ANXs, autologous SN and natural SN implanted subcutaneously in rats for 4 weeks. (C) The number of $CD8^+$ and $CD68^+$ cells in ANXs implanted subcutaneously in rats for 4 weeks. Data are presented as the mean ± SD (n = 5). Statistical analysis: n.s. no significances, $^{**}p < 0.01$, $^{*}p < 0.05$.

as a small number of $CD4^+$ T cells. In the CD NG group, moderate amounts of $CD8^+$ T cells and $CD68^+$ macrophages were detected ($CD8^+$: 68.74 ± 13.27, $CD68^+$: 54.28 ± 10.53), but no $CD4^+$ T cells were detected. In the CD+$scCO_2$ NG group, similar test results appeared, except that the number of $CD8^+$ T cells and $CD68^+$ macrophages was smaller ($CD8^+$: 22.35 ± 6.76, $CD68^+$: 17.16 ± 5.34), and $CD4^+$ T cells were not detected. In addition, we counted the number of $CD8^+$ T cells and $CD68^+$ macrophages in the two ANXs groups and found that there were significant differences between the two ANXs groups ($p < 0.01$) (Fig. 7C).

3.8. Motor function recovery and histological evaluation of target muscle

Using the Catwalk XT 10.6 footprint collection and analysis system, we analyzed the recovery of motor function in the injured limbs in rats after ANXs bridging. Fig. 8A (left) shows the real-time footprints of each group of rats in the gait collection device at 12 weeks after the operation. The fluorescent green footprints in the white dashed frame are the

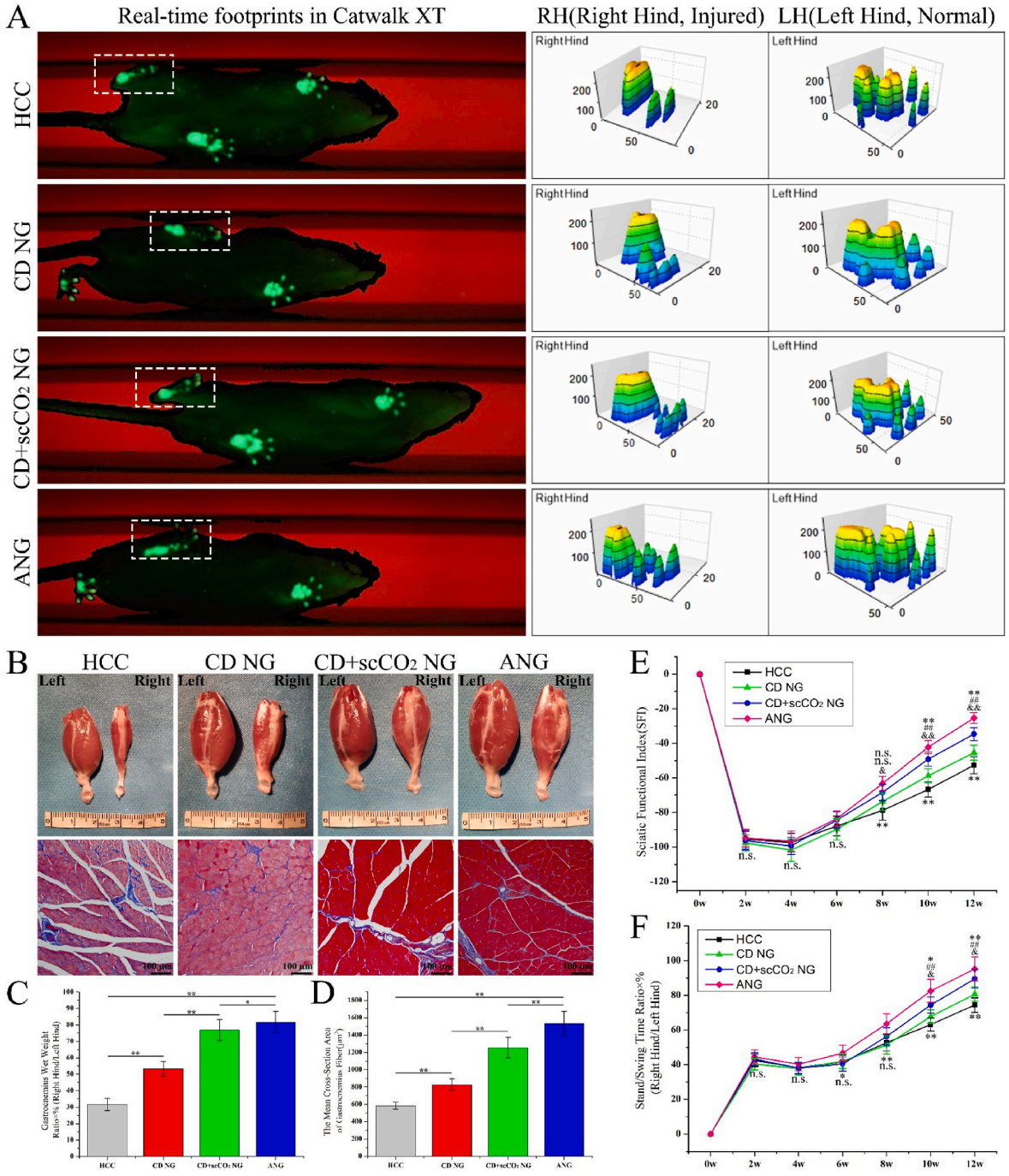

Fig. 8. Evaluation of motor function recovery and target muscle histology. (A) The real-time footprints of three-dimensional stress diagrams of each group of rats in the gait collection device at 12 weeks after the operation. (B) The gross view and Masson staining of the gastrocnemius muscle of each group of rats at 12 weeks postoperatively. (C, D) The wet weight ratio of the gastrocnemius and the mean cross-sectional area of gastrocnemius fibers at 12 weeks postoperatively. Data are presented as the mean ± SD (n = 5). (E, F) The sciatic nerve function index (SFI) and the standing/swing time ratio of each group of rats every 2 weeks after the operation until 12 weeks after the operation. Data are presented as the mean ± SD (n = 5). Statistical analysis: n.s. no significances, (**, ##, &&) $p < 0.01$, (*, #, &) $p < 0.05$.

injured hind of the rats. The toes of the ANG group were fully expanded, while the HCC group had no obvious toe imprints, and the two ANXs groups had obvious toe imprints that were not fully expanded. Analyzing at the real-time footprint of the rat, the gait analysis system collected the pressure data of the footprint and provided the corresponding 3D stress map (Fig. 8A, right). The left hind foot of rats in all groups were on the uninjured side, the force area of the footprints was large, and the obvious stress peaks of the heel and toes were visible. The right hind limb is the injured side, and its 3D stress map showed the same trend as the real-time footprint. In addition, to continuously and dynamically evaluate the recovery of motor function in injured limbs in rats, we evaluated the SFI and the standing/swing time ratio of each group of rats every 2 weeks after the operation until 12 weeks after the operation.

In the first 6 weeks after surgery, the ANG group displayed the highest SFI value, and the CD NG group exhibited the lowest SFI value (Fig. 8E). However, there was no significant difference in SFI between the groups. Starting from the 8th week after surgery, the SFI value of the CD NG group (−73.74 ± 5.11) began to exceed that of the HCC group (−78.85 ± 5.62), and the SFI between the groups began to show significant differences. At the same time, starting from the 8th week after surgery, the SFI value of each group increased rapidly in the order of ANG first, CD + $scCO_2$ NG second, CD NG third, and HCC fourth.

For the standing/swing time ratio (Fig. 8F), in the first 4 weeks after surgery, the ANG group had the highest value, and the CD NG group had the lowest value. However, there was no significant difference between the four groups. At the 6th week after surgery, the CD + $scCO_2$ NG group had the lowest value (40.38 ± 4.14%). Although there were significant differences among the four groups ($p = 0.03$), there was no significant difference between the first three groups (HCC, CD NG and CD + $scCO_2$ NG: $p = 0.73$). At the 8th week after surgery, the CD + $scCO_2$ NG group (56.29 ± 4.97%) surpassed the CD NG group (with the lowest value: 51.46 ± 5.32%). Although there were significant differences among the four groups ($p < 0.001$), there was still no significant difference between the first three groups ($p = 0.16$). At the 10th week after the operation, the CD NG group (67.69 ± 3.82%) surpassed the HCC group (63.15 ± 3.79%), and significant differences began to appear between the groups. The trend between the groups at the 12th week after the operation remained consistent with that at the 10th week.

For the target muscle, we measured the wet weight ratio of the gastrocnemius and the mean cross-sectional area of gastrocnemius fibers 12 weeks postoperatively. Compared to the ANG group, the gastrocnemius of the injured limb in the HCC group exhibited a certain degree of atrophy (Masson staining showed more blue-stained collagen fibers), but no significant atrophy was observed in the CD NG or the CD + $scCO_2$ NG group (Fig. 8B). The wet weight ratio of gastrocnemius in the HCC group was the lowest (31.63 ± 3.77%), the ANG group was the highest (81.57 ± 6.54%), and the CD + $scCO_2$ NG group (76.84 ± 6.38%) was close to the ANG group and higher than the CD NG group (53.28 ± 4.62%), and there were significant differences between the groups ($p < 0.05$) (Fig. 8C). Similarly, the mean cross-sectional area of gastrocnemius fibers in the HCC group was the lowest (584.36 ± 42.74 μm^2), the ANG group was the highest (1532.88 ± 138.81 μm^2), the CD + $scCO_2$ NG group (1255.29 ± 117.85 μm^2) was higher than the CD NG group (827.63 ± 67.46 μm^2), and there were significant differences among the groups ($p < 0.01$) (Fig. 8D).

3.9. Evaluation of the quality of regenerated nerves

Combining HE staining of the ANXs subcutaneously implanted into the rat in this experiment and previously published research [1], we believe that 3 weeks is the best time point to evaluate the extension of the new axon in the nerve graft in the rat 15 mm nerve defect model. Therefore, we took the bridging segment of 1 rat in the experimental groups (CD NG and CD + $scCO_2$ NG) 3 weeks after the operation and performed longitudinal sectioning and NF200 immunofluorescence staining to observe the extension of the regenerated nerve fibers inside the ANXs. As shown in Fig. 9A, the swelling on the left side of the graft segment is the proximal suture. The bright green new nerve fibers basically crossed the graft segment, and the new nerve fibers were less distributed in the middle part of the graft, which primarily grew close to the inner wall of the CD + $scCO_2$ NG. Since the longitudinal slice operation of the transplanted segment of the CD NG group failed, it is not shown here.

We opened the surgical incisions of all remaining rats 12 weeks after the operation. The general view of the grafts in each group is shown in Fig. 9B. The chitosan tube wall in the HCC group began to show signs of degradation. The graft segments in the CD NG group exhibited varying degrees of light yellow, while the graft segments in the CD + $scCO_2$ NG and ANG groups were milky white, which was close to naive nerve morphology. The cross-sectional immunofluorescence of the farthest part of the graft segments in each group showed that the diameter of the regenerating nerve axons in the HCC group was relatively thin and distributed randomly in a star-like manner. In sharp contrast, the regenerative nerve axons in the ANG group were thick in diameter and arranged regularly, and the green myelin sheath surrounding the axons was thicker. Compared to the HCC group, the regenerative nerve axons in the CD NG group were slightly larger in diameter, but they were still irregularly distributed. The diameter of regenerative nerve axons in the CD + $scCO_2$ NG group was larger than that in the CD NG group, close to the ANG group, and exhibited a clustered distribution.

Furthermore, we created semi-thin sections and performed toluidine blue staining on the cross-sections of the farthest sections of the grafts in each group, and the morphology was similar to the results of immunofluorescence staining. It should be noted that there were increased dark blue ribbon-like collagen fibers in the CD NG group. We quantified the density of myelinated nerve fibers in each group (Fig. 9C): The CD NG group (7483.95 ± 402.38/mm^2) was higher than the HCC group (with the lowest value: 7045.27 ± 384.61/mm^2, $p = 0.0011$). The CD + $scCO_2$ NG group (8134.74 ± 420.86/mm^2) was higher than the CD NG group ($p < 0.001$) and higher than the ANG group (8066.77 ± 395.29/mm^2), but there was no significant difference between the two groups (CD + $scCO_2$ NG *vs.* ANG: $p = 0.6016$).

Finally, to evaluate the diameter of the nerve fibers and the thickness of the myelin sheath in each group, we created ultrathin sections on the cross section of the farthest part of the graft. Regarding the diameter of regenerated nerve fibers in each group (Fig. 9D), the diameter of the CD NG group (4.51 ± 0.32 μm) was higher than that of the HCC group (with the lowest value: 4.15 ± 0.36 μm, $p = 0.0019$). The CD group (5.98 ± 0.47 μm) was close to the ANG group (6.52 ± 0.44 μm, $p = 0.0006$) and higher than the CD NG group (*vs.* CD + $scCO_2$ NG: $p < 0.001$), and there were significant differences among the groups. Regarding the thickness of the myelin sheath of the regenerated nerve fibers in each group (Fig. 9E), the trend of the statistical results between the groups (HCC: 0.68 ± 0.11 μm, CD NG: 0.98 ± 0.16 μm, CD + $scCO_2$ NG: 1.69 ± 0.18 μm, ANG: 1.85 ± 0.21 μm) was similar to the diameter of the regenerated nerve fibers, and there were significant differences among the groups ($P < 0.05$).

4. Discussion

Severe peripheral nerve injury with nerve defects are heavy medical and social burdens. At the same time, the treatment costs are expensive and cannot be accepted by most patients, while treatment efficacy remains limited [4]. Therefore, in the current medical environment, autologous nerve transplantation is still the first choice of many patients and doctors, despite its many shortcomings [3]. To overcome these shortcomings, a variety of artificial nerve grafts have been developed and continuously optimized. Among them, ACNGs, which are closest to natural nerves in structure and composition, are a very promising alternative to autologous nerve grafts. In addition, the development of cross-disciplines and the comprehensive application of multifield

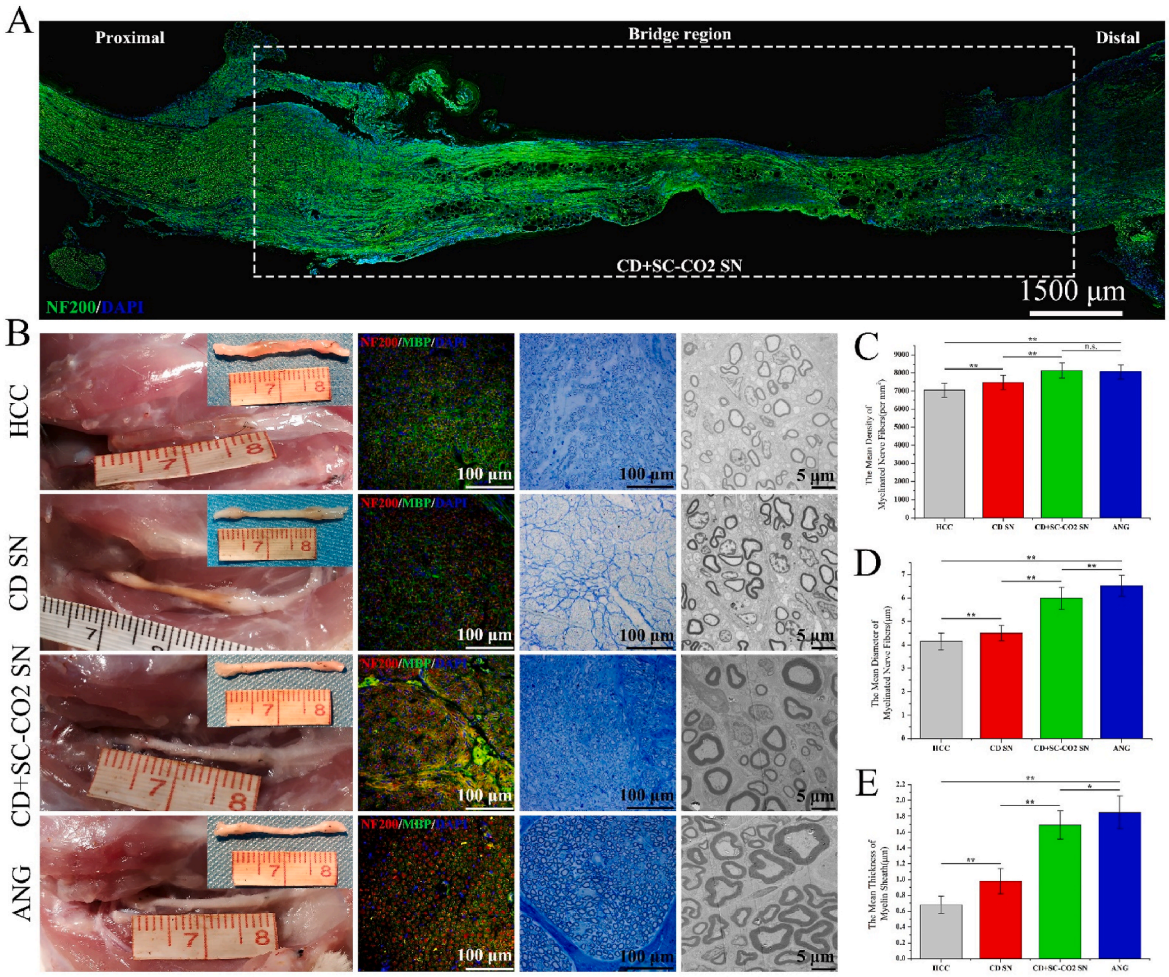

Fig. 9. Evaluation of the quality of regenerated nerves.
(A) Longitudinal neurofilament 200 immunofluorescence staining (NF200: green, DAPI: blue) of the grafting segment in the CD + $scCO_2$ NG group 3 weeks after the operation is shown. (B) The general view of the nerve grafts in each group at 12 weeks after the operation, as well as the immunofluorescence (NF200: red, MBP: green, DAPI: blue), toluidine blue staining and transmission electron microscopy (TEM) images of the farthest sections of the grafts. (C, D, E) The mean density and diameter of myelinated nerve fibers and the mean thickness of the myelin sheath in each group. Data are presented as the mean ± SD (n = 10). Statistical analysis: n. s. no significances, $^{**}p < 0.01$, $^{*}p < 0.05$. (For interpretation of the references to color in this figure legend, the reader is referred to the Web version of this article.)

technologies provide new opportunities for the preparation of decellularized nerve grafts with improved performance. Based on the anatomical characteristics of large mammalian peripheral nerves and the various advantages of $scCO_2$ extraction technology, we believe that $scCO_2$ extraction is the best choice for preparing ANXs derived from porcine peripheral nerves. To the best of our knowledge, this is the first report describing the use of $scCO_2$ extraction technology to prepare ACNGs. In this study, we prepared ANXs derived from porcine sciatic nerves using a comprehensive program combining physical and chemical technologies such as repeated freezing and thawing, chemical detergents, ultrasonic cleaning, DNA/RNase and supercritical extraction. A comprehensive and systematic evaluation of ANXs revealed that the fat content of the CD + $scCO_2$ NG was removed to the greatest extent, and its DNA content was also reduced to below clinical standards. At the same time, the in vitro experiment of inoculating DRG on ANXs membrane showed that nerve axons on CD + $scCO_2$ NG can grow naturally and extended a long distance. In vivo, ANXs was subcutaneously transplanted into rats and dynamically observed for 4 weeks, and the results of HE and immunohistochemistry showed that CD + $scCO_2$ NG only caused a very weak inflammatory response. Second, ANXs was used to bridge 15 mm sciatic nerve defects in rats, and the repair effects were evaluated in terms of regenerated nerve quality, target muscle wet weight and motor function recovery. The results showed that CD + $scCO_2$ NG was similar to autologous nerves and was significantly better than hollow NGCs and CD NG.

Literature shows that the current preparation schemes of decellularized nerve grafts mostly use a single chemical detergent or the comprehensive application of multiple chemical detergents [1,68–70]. The technology of a single chemical detergent in preparing ACNGs with smaller diameters and fewer nerve bundles has been developed, and there are a large number of relevant basic studies, such as in the sciatic nerve of rats. Peripheral nerves derived from porcine sources have the characteristics of thicker diameter, dense epineurium and increased nerve bundles. Therefore, it is difficult for a single chemical detergent to achieve a satisfactory decellularization effect, and the processing cycle is long. In addition, the combination of multiple chemical detergents increases the possibility of chemical reagent residue. Based on the above description, we chose the composite scheme based on $scCO_2$ extraction to decellularize the porcine sciatic nerve (Fig. 1). Chemical detergent has a good effect on removing genetic material from tissues, which has been recognized by most researchers [33,71]. In this study, the DNA content of porcine sciatic nerves treated with SDS decreased from 3725.73 ± 242.31 ng/mg to 52.28 ± 3.58 ng/mg (Fig. 3H). In addition, most of the acellular schemes reported in the literature are still based on chemical detergent, which has also been proven [33]. Therefore, in this study, we chose a chemical detergent, SDS, and applied it to the

decellularization process at a very low concentration (0.5%). Importantly, although SDS is a mild ionic detergent, it denatures the protein by destroying the structure of the protein at an inappropriate concentration [72,73]. In addition, for lipophilic compounds, organic solvents do have a good degreasing effect [74]. However, most of the organic solvents have strong biological toxicity and are easy to adhere to the surface and interior of biological materials (especially ECM-based materials) and are difficult to remove. The main reason is that this ECM-based material is rich in a variety of proteins with the characteristics of easy adhesion, and has a complex surface topology that is not conducive to the separation of organic solvents [75,76]. It is gratifying that supercritical carbon dioxide extraction technology perfectly avoids the disadvantages of organic solvents, and has natural lipophilicity, so it is the perfect choice to replace organic solvents for degreasing of biological materials. The scheme of placing the $scCO_2$ extraction step after the chemical detergent is the result of our comprehensive consideration based on the following observations: I) The porous structure formed after the nerve tissue undergoes chemical decellularization treatment is conducive to the entry of $scCO_2$, which improves the extraction efficiency [51]. II) Studies have shown that $scCO_2$ can be used to decellularize tissues, so it removes cellular debris and genetic material remaining after chemical detergent treatment while defatting [53,54]. III) $scCO_2$ is a good solvent for many substances, so it may play a role in removing chemical detergents remaining in ACNGs [41]. Ⅳ) $scCO_2$ has sterilization properties, so it may have a disinfection effect on the incorporation of bacteria in the operation [45].

In view of the excellent performance of $scCO_2$ in dissolving lipids, we also prepared satisfactory ANXs in this study. After 6 cycles of extraction, no extract was discharged from the material receiving port of the supercritical equipment. The fat content of nerve samples after the end of each extraction cycle was then determined. The results showed that the fat content decreased step by step, and finally, the fat content decreased by 59.45% (Fig. 3E). At the same time, after $scCO_2$ extraction, the DNA content of ANXs also decreased from 52.28 ± 3.58 ng/mg to 38.02 ± 3.72 ng/mg (Fig. 3H). In addition, chemical detergents have a weak defatting effect. In this study, after chemical detergent treatment, although the difference was not statistically significant, the fat content of ANXs decreased by 6.47% (Fig. 3F). In general, chemical detergents are effective in removing genetic material and have a weak defatting effect. $scCO_2$ exhibited a significant effect in defatting and has a certain degree of decellularization. However, two recent studies indicated that a more satisfactory decellularized porcine corneal scaffold and decellularized rat myocardial hydrogel can be obtained by simply relying on $scCO_2$ [53,54]. These research reports are not in conflict with this research because porcine corneal tissue and rat myocardial tissue more easily complete decellularization, and both contain no or only a small amount of adipose tissue. In the food field, to satisfy people's healthy low-fat diet, $scCO_2$ is also used to defat the bovine heart [77]. In addition, the combination of $scCO_2$ and peracetic acid decellularized baby spinach leaves within 4 h, and human fibroblasts can adhere and survive for 14 days after inoculating the surface of spinach leaves [78].

On the other hand, we also evaluated the decellularization and defatting effects morphologically. HE and Oil Red O staining revealed increased nerve bundles and adipose tissue between bundles in fresh porcine sciatic nerves. After chemical detergent treatment, there were no visible blue-stained cell nucleus in CD NG, and there was no changes in red-stained adipose tissue (Figs. 2C and 3A). However, after the $scCO_2$ extraction process, there was no visible red-stained adipose tissue in the CD + $scCO_2$ NG. In addition, immunofluorescence (laminin + DAPI) and HE staining of CD + $scCO_2$ NG exhibited a well-preserved porous neural basement membrane tube structure, indicating that the above composite decellularization scheme based on $scCO_2$ extraction did not cause serious damage to the neural structure (Fig. 2B). In another study on decellularization of porcine peripheral nerves, this well-preserved porous nerve structure could not be seen [62]. We speculate that the use of a variety of chemical reagents destroyed the nerve structure. In recent years, hydrogels have attracted much attention due to their excellent properties, especially xenogeneic acellular matrix hydrogels, which have been used to repair various types of tissue injury [79–82]. On a related note, in the repair of peripheral nerve injury, there are also several reports on heterogeneous acellular matrix hydrogels [71,74]. However, we believe that in the repair of peripheral nerve injury, especially nerve defects, acellular nerve scaffolds have more advantages than hydrogels because well-preserved three-dimensional directional nerve fiber basement membrane tubes provide nanotopological clues for regenerated axons. Interestingly, to compensate for the shortcomings of hydrogels in topological clues, researchers have used electrospinning technology to prepare aligned nanofibers, and acellular matrix hydrogels have been coated on nanofibers to provide chemical clues [71]. Finally, in the experiment of repairing 5 mm sciatic nerve defects in rats, this design also obtained relatively satisfactory results. Hydrogels may play a greater role in peripheral nerve crush injuries [83]. In addition, it should be pointed out that fat grafting has also become increasingly popular in peripheral nerve surgery in recent years [84], which is not contradictory to the operation in this study to reduce the fat content of ANXs by means of scCO2 extraction. On the one hand, the function of adipose tissue in fat grafting is mainly achieved by the adipose-derived stem cells (ADSCs) it contains, which can differentiate into many lineages and secrete neurotrophic and angiogenic factors [85,86]. on the other hand, in order to avoid immune response and to make it easier to pass ethical review, the adipose tissue (ADSCs) involved in peripheral nerve surgery are all autologous fat. Of course, in order to improve the repair effect of long-gap nerve defects, autologous adipose tissue (ADSCs) can also be considered together with the novel acellular nerve ANXs prepared in this study.

The ECM is formed by the combination of substances secreted by resident cells of each tissue and organ in a certain way [56]. Considering that $scCO_2$ is a good solvent for many substances, we wondered whether it also removes some ECM-related components during the process of defatting and decellularization. Therefore, we assessed the expression of major ECM-related proteins in the extract, such as collagen I, II, Ⅳ and fibronectin (Fig. 4A and E). The expression level of collagen Ⅳ in the extract was moderate, while expression levels of other proteins were low; in sharp contrast, expression levels of 4 proteins in the CD + $scCO_2$ NG were higher. The above results indicate that $scCO_2$ has little effect on the primary components related to ECM. Recently, a study from Seo et al. reported that during the process of decellularization, $scCO_2$ protects the ECM structure from damage and retains various angiogenic proteins in the rat heart ECM [54]. Unfortunately, we did not systematically evaluate the factors or proteins related to nerve regeneration, which is a shortcoming of this study. With the help of non-labeled (label-free) protein quantification technology, we analyzed natural SN and two kinds of ANXs. The results of SDS–PAGE showed that compared to natural SN, the protein types of ANXs were relatively reduced, primarily those with a molecular weight of less than 30 kDa (Fig. 4B). Next, using bioinformatics analysis technology, we further analyzed the results. Heatmap analysis showed that most of the highly expressed proteins in natural SN were downregulated in the two ANXs varieties (Fig. 4C). In addition, we focused on DEPs among the three neural tissues (Fig. 4F–I). In essence, the DEPs between natural nerves and CD NG were related to technical operations, such as repeated freezing and thawing, chemical washing, and ultrasonic vibration, while DEPs between CD NG and CD + $scCO_2$ NG were related to the $scCO_2$ extraction procedure. Interestingly, GO and KEGG enrichment analysis of these two types of DEPs revealed that the results were very similar. Specifically, CC was primarily related to cells, cell parts, intracellular parts, intracellular parts and cytoplasm, which are primarily the products of acellular processes. We speculate that $scCO_2$ has a certain degree of decellularization in addition to its primary defatting effect, which is similar to the effect of chemical detergents. Of course, the above results also echo the previous experimental results of reduced DNA content in the CD + $scCO_2$ NG.

After some proteins were removed using the above chemical detergent and $scCO_2$ technologies, some important ECM-related proteins remained in the final ANXs (CD + $scCO_2$ NG). The results of bioinformatics analysis of the protein in the CD + $scCO_2$ NG showed that it was mainly involved in the signaling pathways related to axon guidance and the cAMP signaling pathway in the KEGG pathway (Fig. 4J and K). A recent study showed that compared to spinal cord tissue-derived decellularized hydrogels, peripheral nerve-derived decellularized hydrogels displayed a stronger effect on promoting myelination, which may be related to laminin, collagens and fibronectin [87]. It is undeniable that these proteins were also completely retained in the CD + $scCO_2$ NG in this study. However, for the time being, there is no report that tissue-derived ECM hydrogels can guide nerve regeneration axons. We speculate that the related proteins involved in the axon guidance pathway may be related to the well-preserved three-dimensional directional nerve basement membrane tube structure in the CD + $scCO_2$ NG. All of this is primarily due to $scCO_2$ extraction, the low concentration and milder chemical detergents.

According to previous reports in the literature, we used similar techniques to evaluate the effects of two kinds of ANXs on axons in vitro [1,88]. Specifically, with the help of frozen section technology, we prepared ANXs membranes and inoculated DRGs of rats in or around them. To observe the interaction between fat in ANXs and DRG axons, we first performed immunohistochemical staining of DRGs inoculated on ANXs membranes and then performed Oil red O staining (Fig. 6). Here, we observed a very interesting phenomenon: for DRGs inoculated on the outside of the CD NG membrane, it was difficult for its axons to enter the red-stained adipose zones; a small number of axons that entered the adipose zones grew disorderly and had a tendency to degenerate. In addition, for the DRG inoculated inside the CD NG membrane, its axons were primarily concentrated in the nonadipose zones. When the axon extended from the nonadipose zone to the boundary line of the adipose zone, it obviously turned toward the nonadipose zone. In the gap of the adipose zone, only one axon entered the nonadipose zone after passing through (Fig. 6A). In this regard, we speculated the following two possibilities: I) Due to its hydrophobic characteristics, the biological activity of adipose tissue is limited, which is not conducive to the adhesion or growth of nerve axons [89]. II) Adipose tissue may contain some proteins or factors similar to chondroitin sulfate proteoglycans (CSPG), which inhibit axons [88]. However, for the CD + $scCO_2$ NG membrane that removes adipose tissue to the greatest extent, more nerve axons will enter its interior and extend to the nonadipose zone and the adipose zone before extraction treatment (currently the nonadipose zone) (Fig. 6B). In addition, the statistical results showed that in terms of the extension length of the axons inside the membranes, the axon density at a distance of 0.4 mm from the center of the DRG cell cluster outside the membranes, the number of axons that enter the ANXs membranes by the extramembrane DRG, and the number of axons that turn at a small angle, the CD + $scCO_2$ NG group was better than the CD NG group. However, for DRGs inoculated outside the membrane, there was no significant difference in axon length between the two ANXs. We believe that the anterior region has a smaller angle relative to the posterior region, and the effect of ANXs on axons is offset or compensated for by the posterior region.

Generally, for xenografts, researchers are most worried about biocompatibility and immunogenicity [90]. However, the immunogenicity of tissue-derived ECM grafts after decellularization has been greatly reduced [91,92]. In recent years, biomaterials derived from porcine nerves have been extensively studied and have achieved satisfactory results in nerve repair [71,74,87]. In this study, we seeded Schwann cells on the ANXs scaffold, and the results demonstrated that the number of adherent and growing cells on the CD + $scCO_2$ NG scaffold was greater, and the number of red-stained dead cells was reduced. CCK8 showed similar results. Scanning electron microscopy showed that Schwann cells adhered to the CD + $scCO_2$ NG scaffold at a higher density. In addition, the cells on the CD + $scCO_2$ NG scaffold exhibited a higher secretion level of GDNF and NGF (Fig. 5). We speculate that the main reason for the above results is that the hydrophobic characteristics of adipose tissue and the possible residual chemical detergent in CD NG are not conducive to the adhesion and proliferation of Schwann cells. Several previous studies have evaluated the host immune rejection of pig decellularized nerves, but we have not observed the overall morphology of the graft in the animal body [74,93]. Therefore, in this study, we first performed HE staining of ANXs implanted under the skin of rats (Fig. 7A). The results showed that the autologous nerve as a negative pair maintained better micromorphology, while a large number of neutrophils were observed around and inside the natural porcine nerve. For CD NG, neutrophils aggregate primarily in the adipose zone between nerve bundles. However, there were almost no visible neutrophils in the CD + $scCO_2$ NG 1 week after implantation. These above results suggest that adipose tissue may play an important role in the related immune response of xenogeneic nerve grafts. In addition, according to current research, the relationship between lipids and inflammation in the field of organ transplantation has not been fully elucidated. One study showed the presence of lipoprotein A4 in bronchiolar lavage fluid from lung transplant patients who presented with acute allogeneic rejection, with concentrations correlated with clinicopathological severity [94]. However, it has also been suggested that lipids act on specific receptors to enhance cell arrest, resulting in decreased neutrophil migration [95]. From an immunological point of view, the immune response mediated by xenografts is primarily related to the Th1 and Th2 lymphocyte phenotypes [96]. Allman et al. subcutaneously implanted porcine small intestinal submucosa as a natural acellular extracellular matrix in mice. The results suggested that the immune response induced by it was similar to that of syngeneic tissues, primarily confined to the local and systemic Th2 pathways, consistent with remodeling reactions rather than rejection [97]. However, in this study, we did not detect $CD4^+$ T cells in the other three grafts, only in the natural porcine nerves (Fig. 7B). In the two ANXs groups at the same time point, we detected a number of $CD8^+$ T and $CD68^+$ T cells, which is similar to the results of previous studies [74,93]. Compared to the CD NG, the number of $CD8^+$ T and $CD68^+$ T cells that could be detected in the CD+$scCO_2$ NG was lower, and this difference was significantly different (Fig. 7C). The above results suggest that the host acute inflammatory response caused by CD + $scCO_2$ NG is weaker, and the difference in these experimental results is mainly caused by $scCO_2$ extraction.

In a 3-month experiment of repairing 15 mm nerve defects in rats, the CD + $scCO_2$ NG group exerted superior repair effects in a series of morphological and functional evaluations. Immunofluorescence revealed that the regenerated nerve axons had basically crossed the CD + $scCO_2$ NG 3 weeks after surgery, which may be attributed to the well-preserved three-dimensional oriented structure of the nerve fiber basement membrane tube that can guide nerve regeneration (Fig. 9A). The transplanted segments in the CD NG group 3 months after surgery exhibited varying degrees of light yellow color, which may be an incompletely absorbed inflammatory reaction product caused by immunogenic substances, including a large amount of adipose tissue. However, the graft segment of the CD + $scCO_2$ NG group was similar to that of the ANG group, which appeared milky white and close to naive nerve morphology (Fig. 9B). Regarding nerve regeneration quality parameters (the density and diameter of myelinated nerve fibers and the thickness of the myelin sheath), the CD + $scCO_2$ NG group was close to autologous nerve transplantation and was significantly better than the CD NG and hollow catheter groups (Fig. 9C–E). In addition, in terms of the wet weight of the wet weight ratio of the gastrocnemius and the mean cross-sectional area of gastrocnemius fibers, the recovery among the groups was similar to the above (Fig. 8B–D). Interestingly, the CD NG group had a poor SFI during the first 6 weeks after the operation, which may be related to the early acute inflammatory response. In contrast to autologous nerve transplantation, the CD + $scCO_2$ NG group had poor motor function parameters during the early postoperative period.

However, the recovery of motor function was significantly accelerated in the middle postoperative period (6–8 weeks), and the motor function parameters 12 weeks after surgery were close to those of autologous nerve transplantation (Fig. 8E and F). Finally, it should be noted that compared to the smaller diameter of the rat sciatic nerve, the diameter of the porcine sciatic nerve was larger. Therefore, in the in vivo experiment, we selected the nerve bundle matching the diameter of the rat sciatic nerve. In future experiments, we will continue to use ANX to repair sciatic nerve defects in beagle dogs to evaluate its repair effect in large animals.

5. Conclusion

In summary, using a composite technology based on $scCO_2$ extraction, we obtained an innovative ANX, in which the fat has been removed to the greatest extent, and the DNA content has also been reduced to below clinical standards. More importantly, the well-preserved three-dimensional directional nerve basement membrane tube structure in ANX can better guide and promote the growth of nerve axons. In addition, this is the first study using $scCO_2$ extraction technology to prepare ACNGs for guiding and promoting long-distance nerve regeneration. Finally, we hope that this new type of ANXs based on multifield technology provides scientists with some enlightenment for the design of the next generation of artificial NGCs and the advancement of xenogeneic acellular nerve grafts for clinical application in the near future.

Ethics statement

This study obtained written approval from the Ethics Committee of the Chinese PLA General Hospital, Beijing, China.

Data availability

The data that support this study are available within the article and its Supplementary data files or available from the authors upon request.

CRediT authorship contribution statement

Shuai Wei: Conceptualization, Methodology, Writing – original draft. **Qian Hu:** Methodology, Visualization. **Jianxiong Ma:** Visualization, Investigation. **Xiu Dai:** Data curation. **Yu Sun:** Investigation, Software. **Gonghai Han:** Methodology, Software. **Haoye Meng:** Software, Visualization. **Wenjing Xu:** Investigation. **Lei Zhang:** Investigation, Software. **Xinlong Ma:** Writing – review & editing. **Jiang Peng:** Writing – review & editing. **Yu Wang:** Supervision, Validation.

Declaration of competing interest

The authors declare that they have no known competing financial interests or personal relationships that could have appeared to influence the work reported in this paper.

Acknowledgments

This work was supported by the National Key R&D Program of China (2019YFA0110704), Medical Research and Development Projects (AWS17J005), the National Key R&D Program of China (2017YFA0104702), and we are very grateful to the professional supercritical extraction equipment and technical support provided by Joel Hi-Tech (Dalian, China) Co., Ltd.

Appendix A. Supplementary data

Supplementary data to this article can be found online at https://doi.org/10.1016/j.bioactmat.2022.03.014.

References

[1] X. Sun, Y. Wang, Z. Guo, B. Xiao, Z. Sun, H. Yin, H. Meng, X. Sui, Q. Zhao, Q. Guo, A. Wang, W. Xu, S. Liu, Y. Li, S. Lu, J. Peng, Acellular Cauda Equina allograft as main material combined with biodegradable chitin conduit for regeneration of long-distance sciatic nerve defect in rats, Adv. Healthcare Mater. 7 (17) (2018), e1800276.
[2] A. Magaz, A. Faroni, J.E. Gough, A.J. Reid, X. Li, J.J. Blaker, Bioactive silk-based nerve guidance conduits for augmenting peripheral nerve repair, Adv. Healthcare Mater. 7 (23) (2018), e1800308.
[3] X. Gu, F. Ding, D.F. Williams, Neural tissue engineering options for peripheral nerve regeneration, Biomaterials 35 (24) (2014) 6143–6156.
[4] M.D. Sarker, S. Naghieh, A.D. McInnes, D.J. Schreyer, X. Chen, Regeneration of peripheral nerves by nerve guidance conduits: influence of design, biopolymers, cells, growth factors, and physical stimuli, Prog. Neurobiol. 171 (2018) 125–150.
[5] I.J.-P. J, K. Jansen, A. Gramsbergen, M.F. Meek, Transection of peripheral nerves, bridging strategies and effect evaluation, Biomaterials 25 (9) (2004) 1583–1592.
[6] T.B. Bini, S. Gao, X. Xu, S. Wang, S. Ramakrishna, K.W. Leong, Peripheral nerve regeneration by microbraided poly(L-lactide-co-glycolide) biodegradable polymer fibers, J. Biomed. Mater. Res. 68 (2) (2004) 286–295.
[7] A. Singh, S. Asikainen, A.K. Teotia, P.A. Shiekh, E. Huotilainen, I. Qayoom, J. Partanen, J. Seppälä, A. Kumar, Biomimetic photocurable three-dimensional printed nerve guidance channels with aligned cryomatrix Lumen for peripheral nerve regeneration, ACS Appl. Mater. Interfaces 10 (50) (2018) 43327–43342.
[8] S. Kehoe, X.F. Zhang, D. Boyd, FDA approved guidance conduits and wraps for peripheral nerve injury: a review of materials and efficacy, Injury 43 (5) (2012) 553–572.
[9] M.R. MacEwan, E.R. Zellmer, J.J. Wheeler, H. Burton, D.W. Moran, Regenerated sciatic nerve axons stimulated through a chronically implanted macro-sieve electrode, Front. Neurosci. 10 (2016) 557.
[10] M. Sarker, S. Naghieh, A.D. McInnes, D.J. Schreyer, X. Chen, Strategic design and fabrication of nerve guidance conduits for peripheral nerve regeneration, Biotechnol. J. 13 (7) (2018), e1700635.
[11] B. Sun, Z. Zhou, T. Wu, W. Chen, D. Li, H. Zheng, H. El-Hamshary, S.S. Al-Deyab, X. Mo, Y. Yu, Development of nanofiber sponges-containing nerve guidance conduit for peripheral nerve regeneration in vivo, ACS Appl. Mater. Interfaces 9 (32) (2017) 26684–26696.
[12] L. Yao, G.C. de Ruiter, H. Wang, A.M. Knight, R.J. Spinner, M.J. Yaszemski, A. J. Windebank, A. Pandit, Controlling dispersion of axonal regeneration using a multichannel collagen nerve conduit, Biomaterials 31 (22) (2010) 5789–5797.
[13] T. Yu, Y. Xu, X. Jia, Q. Ao, Intraluminal guiding structure of nerve conduits for peripheral nerve regeneration, Sci. Adv. Mater. 12 (1) (2020) 56–65.
[14] Y. Li, A. Debrot, Fabrication and characterization of a protein composite conduit for neural regeneration, ACS Applied Bio Materials 2 (10) (2019).
[15] J. Wang, H. Xiong, T. Zhu, Y. Liu, H. Pan, C. Fan, X. Zhao, W.W. Lu, Bioinspired multichannel nerve guidance conduit based on shape memory nanofibers for potential application in peripheral nerve repair, ACS Nano 14 (10) (2020) 12579–12595.
[16] S. Vijayavenkataraman, Nerve guide conduits for peripheral nerve injury repair: a review on design, materials and fabrication methods, Acta Biomater. 106 (2020) 54–69.
[17] S. Yang, C. Wang, J. Zhu, C. Lu, H. Li, F. Chen, J. Lu, Z. Zhang, X. Yan, H. Zhao, X. Sun, L. Zhao, J. Liang, Y. Wang, J. Peng, X. Wang, Self-assembling peptide hydrogels functionalized with LN- and BDNF- mimicking epitopes synergistically enhance peripheral nerve regeneration, Theranostics 10 (18) (2020) 8227–8249.
[18] F. Rao, Y. Wang, D. Zhang, C. Lu, Z. Cao, J. Sui, M. Wu, Y. Zhang, W. Pi, B. Wang, Y. Kou, X. Wang, P. Zhang, B. Jiang, Aligned chitosan nanofiber hydrogel grafted with peptides mimicking bioactive brain-derived neurotrophic factor and vascular endothelial growth factor repair long-distance sciatic nerve defects in rats, Theranostics 10 (4) (2020) 1590–1603.
[19] J. Wang, Y. Cheng, H. Wang, Y. Wang, K. Zhang, C. Fan, H. Wang, X. Mo, Biomimetic and hierarchical nerve conduits from multifunctional nanofibers for guided peripheral nerve regeneration, Acta Biomater. 117 (2020) 180–191.
[20] S. Miao, H. Cui, M. Nowicki, L. Xia, X. Zhou, S.J. Lee, W. Zhu, K. Sarkar, Z. Zhang, L.G. Zhang, Stereolithographic 4D bioprinting of multiresponsive architectures for neural engineering, Adv. Biosyst. 2 (9) (2018).
[21] L. Wang, C. Lu, S. Yang, P. Sun, Y. Wang, Y. Guan, S. Liu, D. Cheng, H. Meng, Q. Wang, J. He, H. Hou, H. Li, W. Lu, Y. Zhao, J. Wang, Y. Zhu, Y. Li, D. Luo, T. Li, H. Chen, S. Wang, X. Sheng, W. Xiong, X. Wang, J. Peng, L. Yin, A fully biodegradable and self-electrified device for neuroregenerative medicine, Sci. Adv. 6 (50) (2020).
[22] J.R. Clegg, A.M. Wagner, S.R. Shin, S. Hassan, A. Khademhosseini, N.A. Peppas, Modular fabrication of intelligent material-tissue interfaces for bioinspired and biomimetic devices, Prog. Mater. Sci. 106 (2019).
[23] J. Zeng, Y. Wu, C. Ren, J. Bonanno, A.H. Shen, D. Shea, J.M. Gehrke, K. Clement, K. Luk, Q. Yao, R. Kim, S.A. Wolfe, J.P. Manis, L. Pinello, J.K. Joung, D.E. Bauer, Therapeutic base editing of human hematopoietic stem cells, Nat. Med. 26 (4) (2020) 535–541.
[24] L.H. Pecker, S. Lanzkron, Sickle cell disease, Ann. Intern. Med. 174 (1) (2021). Itc1-itc16.
[25] S.R. Cerqueira, Y.S. Lee, R.C. Cornelison, M.W. Mertz, R.A. Wachs, C.E. Schmidt, M.B. Bunge, Decellularized peripheral nerve supports Schwann cell transplants and axon growth following spinal cord injury, Biomaterials 177 (2018) 176–185.
[26] K.H. Hillebrandt, H. Everwien, N. Haep, E. Keshi, J. Pratschke, I.M. Sauer, Strategies based on organ decellularization and recellularization, Transpl. Int. : Off. J. European Soc. Organ Transplant. 32 (6) (2019) 571–585.

[27] M. Szynkaruk, S.W. Kemp, M.D. Wood, T. Gordon, G.H. Borschel, Experimental and clinical evidence for use of decellularized nerve allografts in peripheral nerve gap reconstruction, Tissue engineering, Part B, Reviews 19 (1) (2013) 83–96.
[28] S.Y. Fu, T. Gordon, The cellular and molecular basis of peripheral nerve regeneration, Mol. Neurobiol. 14 (1–2) (1997) 67–116.
[29] S.M. Azouz, H.D. Lucas, R.C. Mahabir, S.S. Noland, A survey of the prevalence and practice patterns of human acellular nerve allograft use, plastic and reconstructive surgery, Global open 6 (8) (2018), e1803.
[30] R.W. Hiles, Freeze dried irradiated nerve homograft: a preliminary report, Hand 4 (1) (1972) 79–84.
[31] A.K. Gulati, Evaluation of acellular and cellular nerve grafts in repair of rat peripheral nerve, J. Neurosurg. 68 (1) (1988) 117–123.
[32] O. Frerichs, H. Fansa, C. Schicht, G. Wolf, W. Schneider, G. Keilhoff, Reconstruction of peripheral nerves using acellular nerve grafts with implanted cultured Schwann cells, Microsurgery 22 (7) (2002) 311–315.
[33] P.C. Johnson, R.C. Duhamel, E. Meezan, K. Brendel, Preparation of cell-free extracellular matrix from human peripheral nerve, Muscle Nerve 5 (4) (1982) 335–344.
[34] M. Sondell, G. Lundborg, M. Kanje, Regeneration of the rat sciatic nerve into allografts made acellular through chemical extraction, Brain Res. 795 (1–2) (1998) 44–54.
[35] T.W. Hudson, S. Zawko, C. Deister, S. Lundy, C.Y. Hu, K. Lee, C.E. Schmidt, Optimized acellular nerve graft is immunologically tolerated and supports regeneration, Tissue Eng 10 (11–12) (2004) 1641–1651.
[36] L.J. White, A.J. Taylor, D.M. Faulk, T.J. Keane, L.T. Saldin, J.E. Reing, I. T. Swinehart, N.J. Turner, B.D. Ratner, S.F. Badylak, The impact of detergents on the tissue decellularization process: a ToF-SIMS study, Acta Biomater. 50 (2017) 207–219.
[37] N. Rbia, L.F. Bulstra, T.M. Saffari, S.E.R. Hovius, A.Y. Shin, Collagen nerve conduits and processed nerve allografts for the reconstruction of digital nerve gaps: a single-institution case series and review of the literature, World Neurosurgery 127 (2019) e1176–e1184.
[38] J.T. Mauch, A. Bae, V. Shubinets, I.C. Lin, A systematic review of sensory outcomes of digital nerve gap reconstruction with autograft, allograft, and conduit, Ann. Plast. Surg. 82 (4S Suppl 3) (2019) S247–s255.
[39] M.W. McCrary, N.E. Vaughn, N. Hlavac, Y.H. Song, R.A. Wachs, C.E. Schmidt, Novel sodium deoxycholate-based chemical decellularization method for peripheral nerve, tissue engineering, Part C, Methods 26 (1) (2020) 23–36.
[40] P.M. Crapo, T.W. Gilbert, S.F. Badylak, An overview of tissue and whole organ decellularization processes, Biomaterials 32 (12) (2011) 3233–3243.
[41] S.L. Wells, J. DeSimone, CO(2) technology platform: an important tool for environmental problem solving, Angew. Chem. 40 (3) (2001) 518–527.
[42] C.D. Bevan, P.S. Marshall, The use of supercritical fluids in the isolation of natural products, Nat. Prod. Rep. 11 (5) (1994) 451–466.
[43] P.S. Shah, J.D. Holmes, R.C. Doty, K.P. Johnston, B.A. Korgel, Steric stabilization of nanocrystals in supercritical CO2 using fluorinated ligands, J. Am. Chem. Soc. 122 (17) (2000) 4245–4246.
[44] A.I. Cooper, Recent Developments in Materials Synthesis and Processing Using Supercritical CO2, 2001.
[45] N. Ribeiro, G.C. Soares, V. Santos-Rosales, A. Concheiro, C. Alvarez-Lorenzo, C. A. García-González, A.L. Oliveira, A new era for sterilization based on supercritical CO(2) technology, J. Biomed. Mater. Res. B Appl. Biomater. 108 (2) (2020) 399–428.
[46] J.M. Desimone, Z. Guan, C.S. Elsbernd, Synthesis of fluoropolymers in supercritical carbon dioxide, Science 257 (5072) (1992) 945–947.
[47] W. Leitner, Supercritical carbon dioxide as a green reaction medium for catalysis, Accounts of chemical research 35 (9) (2002) 746–756.
[48] B. Subramaniam, R.A. Rajewski, K. Snavely, Pharmaceutical processing with supercritical carbon dioxide, J. Pharmaceut. Sci. 86 (8) (1997) 885–890.
[49] D.M. Casali, R.M. Handleton, M.A. Matthews, A novel supercritical CO 2 -based decellularization method for maintaining scaffold hydration and mechanical properties, J. Supercrit. Fluids (2017), S0896844617302450.
[50] J.L. Wehmeyer, S. Natesan, R.J. Christy, Development of a sterile amniotic membrane tissue graft using supercritical carbon dioxide, Tissue Eng. C Methods 21 (7) (2015) 649–659.
[51] J. Fages, A. Marty, C. Delga, J.S. Condoret, D. Combes, P. Frayssinet, Use of supercritical CO2 for bone delipidation, Biomaterials 15 (9) (1994) 650–656.
[52] K. Sawada, D. Terada, T. Yamaoka, S. Kitamura, T. Fujisato, Cell removal with supercritical carbon dioxide for acellular artificial tissue, J. Chem. Technol. Biotechnol. 83 (6) (2008) 943–949.
[53] Y.H. Huang, F.W. Tseng, W.H. Chang, I.C. Peng, D.J. Hsieh, S.W. Wu, M.L. Yeh, Preparation of acellular scaffold for corneal tissue engineering by supercritical carbon dioxide extraction technology, Acta Biomater. 58 (2017) 238–243.
[54] Y. Seo, Y. Jung, S.H. Kim, Decellularized heart ECM hydrogel using supercritical carbon dioxide for improved angiogenesis, Acta Biomater. 67 (2018) 270–281.
[55] S.S. Connolly, J.J. Yoo, M. Abouheba, S. Soker, W.S. McDougal, A. Atala, Cavernous nerve regeneration using acellular nerve grafts, World J. Urol. 26 (4) (2008) 333–339.
[56] S.F. Badylak, D.O. Freytes, T.W. Gilbert, Extracellular matrix as a biological scaffold material: structure and function, Acta Biomater. 5 (1) (2009) 1–13.
[57] L. Zilic, P.E. Garner, T. Yu, S. Roman, J.W. Haycock, S.P. Wilshaw, An anatomical study of porcine peripheral nerve and its potential use in nerve tissue engineering, J. Anat. 227 (3) (2015) 302–314.
[58] T. Li, Z. Sui, A. Matsuno, H. Ten, K. Oyama, A. Ito, H. Jiang, X. Ren, R. Javed, L. Zhang, Q. Ao, Fabrication and evaluation of a xenogeneic decellularized nerve-derived material: preclinical studies of a new strategy for nerve repair, neurotherapeutics, J. Am. Soc. Experiment. NeuroTherapeutics 17 (1) (2020) 356–370.
[59] J. Seong, Y. Wang, T. Kinoshita, Y. Maeda, Implications of lipid moiety in oligomerization and immunoreactivities of GPI-anchored proteins, J. Lipid Res. 54 (4) (2013) 1077–1091.
[60] N. Daniel, Daniel Mori, James Kreisel, N. Fullerton, W. Derek, Inflammatory triggers of acute rejection of organ allografts, Immunol. Rev. 258 (1) (2014) 132–144.
[61] A. Curtis, C. Chandler, N. Picton, Cell surface lipids and adhesion. III. The effects on cell adhesion of changes in plasmalemmal lipids, J. Cell Sci. 18 (3) (1975) 375–384.
[62] L. Zilic, S.P. Wilshaw, J.W. Haycock, Decellularisation and histological characterisation of porcine peripheral nerves, Biotechnol. Bioeng. 113 (9) (2016) 2041–2053.
[63] Y. Gu, J. Zhu, C. Xue, Z. Li, F. Ding, Y. Yang, X. Gu, Chitosan/silk fibroin-based, Schwann cell-derived extracellular matrix-modified scaffolds for bridging rat sciatic nerve gaps, Biomaterials 35 (7) (2014) 2253–2263.
[64] J.R. Wiśniewski, A. Zougman, N. Nagaraj, M. Mann, Universal sample preparation method for proteome analysis, Nat. Methods 6 (5) (2009) 359–362.
[65] P. Zhang, F. Xue, Y. Kou, Z. Fu, D. Zhang, H. Zhang, B. Jiang, The experimental study of absorbable chitin conduit for bridging peripheral nerve defect with nerve fasciculu in rats, Artif. Cells Blood Substit. Immobilizat. Biotechnol. 36 (4) (2008) 360–371.
[66] M.T. Wolf, C.L. Dearth, C.A. Ranallo, S.T. LoPresti, L.E. Carey, K.A. Daly, B. N. Brown, S.F. Badylak, Macrophage polarization in response to ECM coated polypropylene mesh, Biomaterials 35 (25) (2014) 6838–6849.
[67] N. Mokarram, K. Dymanus, A. Srinivasan, J.G. Lyon, J. Tipton, J. Chu, A. W. English, R.V. Bellamkonda, Immunoengineering nerve repair, Proc. Natl. Acad. Sci. U. S. A. 114 (26) (2017) E5077–e5084.
[68] J.H. Sun, G. Li, T.T. Wu, Z.J. Lin, J.L. Zou, L.J. Huang, H.Y. Xu, J.H. Wang, Y. H. Ma, Y.S. Zeng, Decellularization optimizes the inhibitory microenvironment of the optic nerve to support neurite growth, Biomaterials 258 (2020) 120289.
[69] D. Pan, D.A. Hunter, L. Schellhardt, A. Fuchs, A.E. Halevi, A.K. Snyder-Warwick, S. E. Mackinnon, M.D. Wood, T cells modulate IL-4 expression by eosinophil recruitment within decellularized scaffolds to repair nerve defects, Acta Biomater. 112 (2020) 149–163.
[70] M. Kasper, C. Deister, F. Beck, C.E. Schmidt, Bench-to-Bedside lessons learned: commercialization of an acellular nerve graft, Adv. Healthcare Mater. 9 (16) (2020), e2000174.
[71] C. Zheng, Z. Yang, S. Chen, F. Zhang, Z. Rao, C. Zhao, D. Quan, Y. Bai, J. Shen, Nanofibrous nerve guidance conduits decorated with decellularized matrix hydrogel facilitate peripheral nerve injury repair, Theranostics 11 (6) (2021) 2917–2931.
[72] T.W. Gilbert, T.L. Sellaro, S.F. Badylak, Decellularization of tissues and organs, Biomaterials 27 (19) (2006) 3675–3683.
[73] T. Woods, P.F. Gratzer, Effectiveness of three extraction techniques in the development of a decellularized bone-anterior cruciate ligament-bone graft, Biomaterials 26 (35) (2005) 7339–7349.
[74] T. Lin, S. Liu, S. Chen, S. Qiu, Z. Rao, J. Liu, S. Zhu, L. Yan, H. Mao, Q. Zhu, D. Quan, X. Liu, Hydrogel derived from porcine decellularized nerve tissue as a promising biomaterial for repairing peripheral nerve defects, Acta Biomater. 73 (2018) 326–338.
[75] S. Wang, C. Zhu, B. Zhang, J. Hu, J. Xu, C. Xue, S. Bao, X. Gu, F. Ding, Y. Yang, X. Gu, Y. Gu, BMSC-derived extracellular matrix better optimizes the microenvironment to support nerve regeneration, Biomaterials 280 (2022) 121251.
[76] H. Xing, H. Lee, L. Luo, T.R. Kyriakides, Extracellular matrix-derived biomaterials in engineering cell function, Biotechnol. Adv. 42 (2020) 107421.
[77] M.S. Rahman, K. Gul, H.S. Yang, J. Chun, W.L. Kerr, S.G. Choi, Thermal and functional characteristics of defatted bovine heart using supercritical CO(2) and organic solvent, J. Sci. Food Agric. 99 (2) (2019) 816–823.
[78] A.F. Harris, J. Lacombe, S. Liyanage, M.Y. Han, E. Wallace, S. Karsunky, N. Abidi, F. Zenhausern, Supercritical carbon dioxide decellularization of plant material to generate 3D biocompatible scaffolds, Sci. Rep. 11 (1) (2021) 3643.
[79] F. Pati, T.H. Song, G. Rijal, J. Jang, S.W. Kim, D.W. Cho, Ornamenting 3D printed scaffolds with cell-laid extracellular matrix for bone tissue regeneration, Biomaterials 37 (2015) 230–241.
[80] L.T. Saldin, M.C. Cramer, S.S. Velankar, L.J. White, S.F. Badylak, Extracellular matrix hydrogels from decellularized tissues: structure and function, Acta Biomater. 49 (2017) 1–15.
[81] R.M. Wang, K.L. Christman, Decellularized myocardial matrix hydrogels: in basic research and preclinical studies, Adv. Drug Deliv. Rev. 96 (2016) 77–82.
[82] G.R. Fercana, S. Yerneni, M. Billaud, J.C. Hill, P. VanRyzin, T.D. Richards, B. M. Sicari, S.A. Johnson, S.F. Badylak, P.G. Campbell, T.G. Gleason, J.A. Phillippi, Perivascular extracellular matrix hydrogels mimic native matrix microarchitecture and promote angiogenesis via basic fibroblast growth factor, Biomaterials 123 (2017) 142–154.
[83] T.L. Lopez-Silva, C.D. Cristobal, C.S. Edwin Lai, V. Leyva-Aranda, H.K. Lee, J. D. Hartgerink, Self-assembling multidomain peptide hydrogels accelerate peripheral nerve regeneration after crush injury, Biomaterials 265 (2021) 120401.
[84] A. Podsednik, R. Cabrejo, J. Rosen, Adipose tissue uses in peripheral nerve surgery, Int. J. Mol. Sci. 23 (2) (2022).
[85] N. Naderi, E.J. Combellack, M. Griffin, T. Sedaghati, M. Javed, M.W. Findlay, C. G. Wallace, A. Mosahebi, P.E. Butler, A.M. Seifalian, I.S. Whitaker, The regenerative role of adipose-derived stem cells (ADSC) in plastic and reconstructive surgery, Int. Wound J. 14 (1) (2017) 112–124.

[86] L. Jiang, T. Mee, X. Zhou, X. Jia, Augmenting Peripheral Nerve Regeneration with Adipose-Derived Stem Cells, Stem Cell Reviews and Reports, 2021.
[87] J.o. Zou, S. Liu, J. Sun, W. Yang, Y.h. Zeng, Peripheral nerve-derived matrix hydrogel promotes remyelination and inhibits synapse formation, Adv. Funct. Mater. 28 (13) (2018).
[88] J.L. Zou, J.H. Sun, S. Qiu, S.H. Chen, F.L. He, J.C. Li, H.Q. Mao, X.L. Liu, D.P. Quan, Y.S. Zeng, Q.T. Zhu, Spatial distribution affects the role of CSPGs in nerve regeneration via the actin filament-mediated pathway, Exp. Neurol. 307 (2018) 37–44.
[89] P. Nooeaid, V. Salih, J.P. Beier, A.R. Boccaccini, Osteochondral tissue engineering: scaffolds, stem cells and applications, J. Cell Mol. Med. 16 (10) (2012) 2247–2270.
[90] C.L. Kaufman, B.A. Gaines, S.T. Ildstad, Xenotransplantation, Ann. Rev. Immunol. 13 (1995) 339–367.
[91] E. Allaire, P. Bruneval, C. Mandet, J.P. Becquemin, J.B. Michel, The immunogenicity of the extracellular matrix in arterial xenografts, Surgery 122 (1) (1997) 73–81.
[92] M.L. Wong, L.G. Griffiths, Immunogenicity in xenogeneic scaffold generation: antigen removal vs. decellularization, Acta Biomater. 10 (5) (2014) 1806–1816.
[93] Y. Zhang, H. Luo, Z. Zhang, Y. Lu, X. Huang, L. Yang, J. Xu, W. Yang, X. Fan, B. Du, P. Gao, G. Hu, Y. Jin, A nerve graft constructed with xenogeneic acellular nerve matrix and autologous adipose-derived mesenchymal stem cells, Biomaterials 31 (20) (2010) 5312–5324.
[94] B.D. Levy, Q.Y. Zhang, C. Bonnans, V. Primo, J.J. Reilly, D.L. Perkins, Y. Liang, M. Amin Arnaout, B. Nikolic, C.N. Serhan, The endogenous pro-resolving mediators lipoxin A4 and resolvin E1 preserve organ function in allograft rejection, Prostaglandins, leukotrienes, and essential fatty acids 84 (1–2) (2011) 43–50.
[95] C.N. Serhan, N. Chiang, T.E. Van Dyke, Resolving inflammation: dual anti-inflammatory and pro-resolution lipid mediators, Nat. Rev. Immunol. 8 (5) (2008) 349–361.
[96] S.F. Badylak, T.W. Gilbert, Immune response to biologic scaffold materials, Semin. Immunol. 20 (2) (2008) 109–116.
[97] A.J. Allman, T.B. McPherson, S.F. Badylak, L.C. Merrill, B. Kallakury, C. Sheehan, R.H. Raeder, D.W. Metzger, Xenogeneic extracellular matrix grafts elicit a TH2-restricted immune response, Transplantation 71 (11) (2001) 1631–1640.